e-palli

AMERICAN JOURNAL OF ENERGY AND NATURAL RESOURCES (AJENR)

ISSN: 2835-9186 (ONLINE)

VOLUME 3 ISSUE 1 (2024)

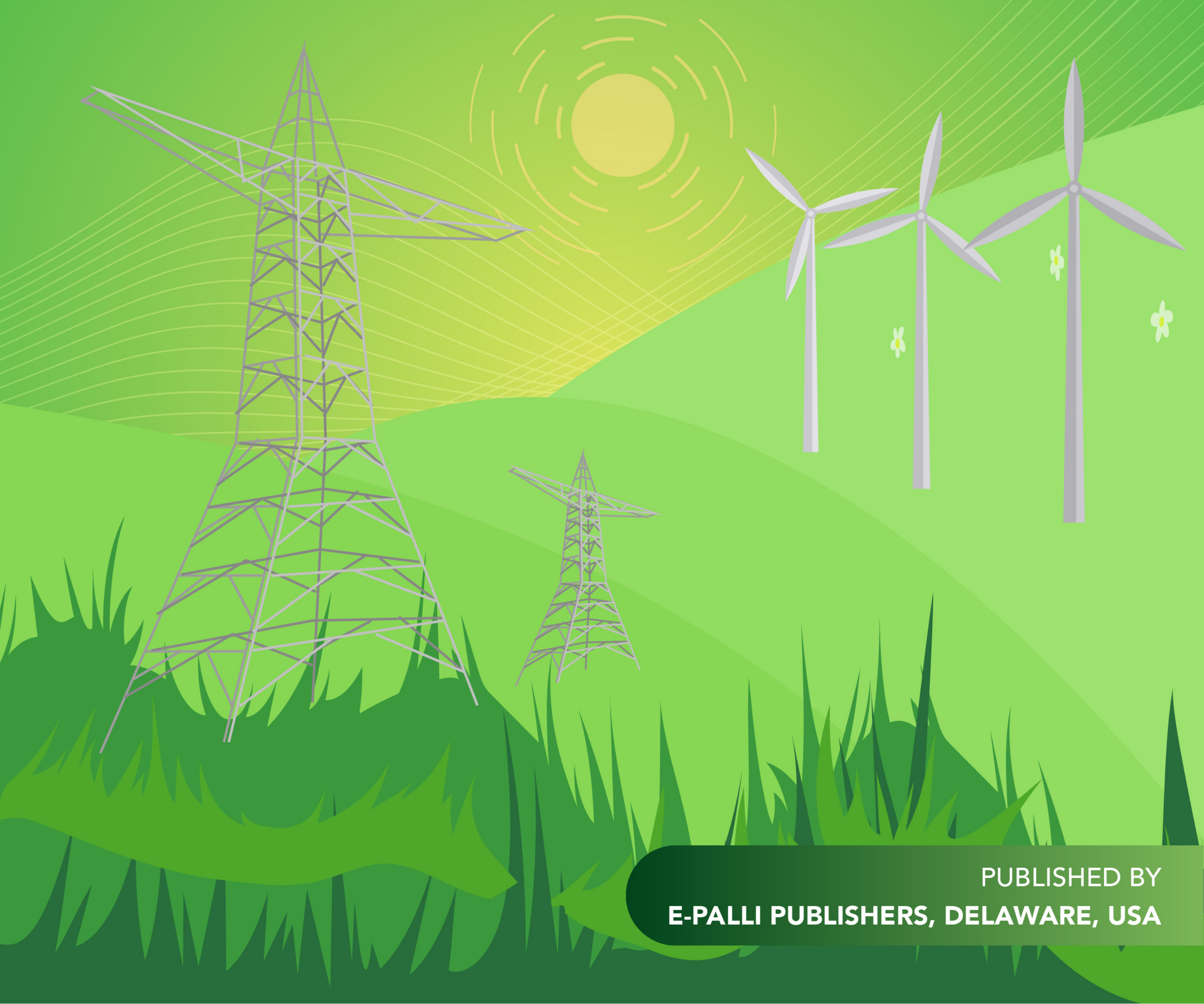

PUBLISHED BY
E-PALLI PUBLISHERS, DELAWARE, USA

American Journal of Energy and Natural Resources (AJENR)

Volume 3 Issue 1, Year 2024
ISSN: 2835-9186 (Online)
DOI: https://doi.org/10.54536/ajenr.v3i1.2569
https://journals.e-palli.com/home/index.php/ajenr

Quantifying the Variability of Solar Energy Fluctuations at High–Frequencies through Short-Scale Measurements in the East–Channel of Mozambique Conditions

Fernando V. Mucomole[1*], Carlos S. A. Silva[2], Lourenço L. Magaia[3]

Article Information

Received: February 29, 2024

Accepted: April 04, 2024

Published: April 07, 2024

Keywords

Fluctuations, High–Frequency, Variability, Solar Energy, Irradiance

ABSTRACT

The solar power output of a solar plant is directly affected by changes in solar energy. To enhance the accuracy, durability, and efficiency of solar projections, it was necessary to quantify the rapid fluctuations in solar energy on a short–scale in the conditions of eastern Mozambique. An analytical approach was utilized to measure the high–frequency variations in the clear–sky index (K^*_t) and its increments (ΔK^*_t). The results indicate that the K^*_t fluctuations in the nine stations along the eastern–channel of Mozambique ranged from 0.0001 to 0.9999, with a probability density (PDF) of fluctuations limited to 0.9991. Through statistical analysis, it was determined that ΔK^*_t reaches its maximum value near zero. Days with intermediate–sky conditions exhibited high PDF values of approximately 1.0 and greater deviation, while clear and cloudy–sky days displayed consistent solar energy frequencies and a lower tendency for K^*_t deviation. In conclusion, the correlation between high–fluctuation variability diminishes rapidly for shorter intervals. Furthermore, high–frequencies of fluctuations are observed during the hot and rainy season, whereas low frequencies are observed during the cold and dry season.

INTRODUCTION

The sun, which serves as the life–giving force for humanity, possesses energy resources that can be deemed limitless. With a diameter of approximately 1.39×10^9 m, it resides at an average distance of about 1.5×10^{11} m from Earth (Duffie & Beckman, 1991). The solar radiation that reaches the earth's surface exhibits a maximum flux density of roughly $1.0\times kWh/m^2$ within the wavelength range of 0.3 to 2.5µm (Twidell & Weir, 2015). As this radiant beam emitted by the sun penetrates the earth, it undergoes division into two components due to interactions with the earth's atmosphere. One component is direct, while the other is diffuse and scatters through the atmosphere (Duffie & Beckman, 1991). Consequently, solar energy experiences intermittency due to various physical phenomena that contribute to its intensity reduction. Gases, solid particles, moving clouds, and other factors cause fluctuations in photovoltaic (PV) generation, leading to fluctuations in irradiance and solar power ramps throughout the day (Halász & Malachi, 2014; Mbaye, 2022). These fluctuations can potentially impact the stability of the grid (J. M. Gomes *et al.*, 2011; G. Lohmann, 2018; Mucomole *et al.*, 2023; Perpiñán & Lorenzo, 2011).

Recent studies have examined the uncertainties associated with predicting solar electricity yield based on fluctuations in solar radiation. These studies have found that there are specific temporal and geographic patterns that can impact the financing of large PV systems and the management of distributed electricity generation (Suri *et al.*, 2007; Woyte *et al.*, 2007). For instance, research conducted has modeled the temporal variability of solar energy availability and observed that clear–sky index (K^*_t) values reach their minimum in July and maximum in December (Mucomole *et al.*, 2023; M. J. R. Perez & Fthenakis, 2015; G. M. Lohmann *et al.*, 2016). Additionally, investigations into solar irradiance fluctuations have revealed the presence of strong short–term nonlinearity, with both linear and nonlinear correlations contributing to the multifractal and nonlinear behavior of solar irradiance (Madanchi *et al.*, 2017; Mucomole *et al.*, 2023). Storage requirements for PV power ramp rate control have also been assessed, highlighting the uncertainties associated with storage. Furthermore, variations in solar radiation and regional precipitation have been evaluated, demonstrating that correlations align with periods of negative irradiance differences during dry high–pressure developments and positive differences during humid low–pressure developments (Perr, 1994; D. Kumar, 2021; Hoff & Perez, 2010). The performance of control strategies for smoothing the active power of PV systems with energy storage has been analyzed, revealing significant differences in estimated degradation between these strategies (Diaz, 2019; Tiba *et al.*, 2016; C. C. C. Gomes *et al.*, 2020). A solar wind model was constructed using the power spectrum of the fluctuations. The analysis, which included heat addition or other types of momentum addition, aimed to achieve better agreement with observations (Tu, 1987; Lave *et al.*, 2012; Siebentritt, 2011; Rapti, 2000; Jamaly, 2020). Additionally, the prediction of solar radiation

[1] Eduardo Mondlane University, Faculty of Engineering, CS-OGET-Center of Excellence of Studies in Oil and Gas Engineering and Technology, Mozambique Avenue km 1.5, Maputo, Mozambique
[2] University of Lisbon, Instituto Superior Técnico, Department of Mechanical Engineering, Portugal, Lisbon
[3] Eduardo Mondlane University, Faculty of Sciences, Department of Mathematics and Informatics, Main Campus, 3453, Maputo, Mozambique
[*] Corresponding author's email: fernandomucomole1@gmail.com

was made, and it was concluded that there are methods available for predicting solar radiation and generation for PV systems (Domingos *et al.*, 2020; Zhang & Yan, 2022; Mills, 2010; Majzoobi & Khodaei, 2016; Soubdhan *et al.*, 2009; Alva *et al.*, 2017). Furthermore, an analysis was conducted to assess the impact of solar irradiance fluctuation on direct osmotic backwash, potentially leading to increased reliability and robustness of battery–free PV membrane systems (Cai & Schäfer, 2020; Zhang & Yan, 2022).

The impact of capacity and remuneration on the utilization of solar energy and wind energy was analyzed. It was determined that the installed capacity must not surpass 5% of the short–circuit level of the grid into which the energy will be fed (Ocácia & Santos, 2008; Hollands *et al.*, 1989; Park *et al.*, 2001; Tiba *et al.*, 2016). Furthermore, the researchers successfully managed the operation of a hybrid PV/diesel generation system, leading to reduced fuel consumption and battery storage requirements, thus confirming the validity of their research (Park *et al.*, 2001; Lan *et al.*, 2018; Jain *et al.*, 2020; Sha & Aiello, 2018). Lastly, an estimation of the output of PV power generation was made based on solar irradiation and frequency classification. The study concluded that the estimation error is approximately 3-4% of the installed capacity of the PV system (Attaviriyanupap *et al.*, 2011). Various approaches were evaluated in order to minimize the effects of rising PV power on voltage fluctuations. It was concluded that cost optimization can be attained by implementing different degrees of PV penetration (D. S. Kumar *et al.*, 2022). Dynamic harmonic regression was utilized to forecast short–term solar irradiation in a separate study. The findings indicated that this method resulted in the lowest relative mean squared error, particularly at approximately 30% and 47% for GHI during a 24–hour prediction (Trapero *et al.*, 2015). The evaluation of high–frequency irradiance fluctuations and geographic smoothing, revealed that smaller scattering factors result in greater reductions in variability compared to the model at longer time scale (Lave *et al.*, 2012; Sha & Aiello, 2020; Behr *et al.*, 2021; Syed & Khalid, 2021; Elfeky *et al.*, 2023). Furthermore, an analysis and statistical examination of fluctuations in the instantaneous clearness–index (K_t) were performed by leading to the identification of statistically significant mean squared values of fluctuations depending on their persistence (Woyte *et al.*, 2007; Lave *et al.*, 2012; Anvari *et al.*, 2016; Alam *et al.*, 2014; Akuffo & Brew-Hammond, 1993). Similarly conducted an analysis and statistical assessment of fluctuations in the instantaneous K_t, concluding the existence of statistically significant mean quadratic values of the fluctuations depending on their persistence (Woyte *et al.*, 2007; Woyte *et al.*, 2006; Ocácia & Santos, 2008; D. S. Kumar *et al.*, 2022). It was determined that high–frequency irradiance fluctuations and geographic smoothing resulted in greater reductions in variability compared to the model at smaller scattering factors and longer time scales (Lave *et al.*, 2012). Lastly, conducted a comprehensive analysis of the fluctuation characteristics of solar energy and the integration of wind–PV systems with Hydrogen (Chen *et al.*, 2022). The study concluded that the unit cost of hydrogen production and the CO_2 emission intensity of wind–PV energy are significantly lower in the system with complementary coupled solar hydrogen production compared to the non-complementary system (Tiba *et al.*, 2016; Exell, 1976).

These traces represent actual variations in solar potential across different regions, resulting from a range of factors such as atmospheric and instrumental interference, as well as research errors. However, they can be interpreted as fluctuations in the amount of solar energy reaching the earth's surface, which can impact the efficiency of PV plants. The eastern–channel of Mozambique, located close to the equator, benefits from a high climate potential and abundant solar resources. Meeting the current demands for housing a larger population, particularly in rural areas where around 85% lack access to conventional electricity, is a key objective of the Sustainable Development Goals (SDGs) for achieving total electrification by 2030. It is important to note that Mozambique is not the only region facing this challenge, as there are other parts of the world with a significant population lacking access to electricity. The effectiveness of both small and large–scale PV projects is being affected by the need to identify optimal periods of the year with minimal fluctuations, given the dynamic variations and increasing climate changes that impact the output power of PV generators. High–frequency fluctuations in solar energy are more prevalent during humid and rainy periods, while intermediate densities occur during seasonal transitions, and low densities are observed during dry and cold seasons.

The objective of this study is to quantify high–frequency fluctuations in solar energy variability along the eastern–channel of Mozambique. By analyzing the Global Horizontal Irradiation (GHI) resource data collected between 2012 and 2014 in various provinces, including Maputo, Gaza, Inhambane, Sofala, Manica, and Tete, we aim to identify periods of low and high fluctuations in solar energy. This information will be crucial for sizing autonomous PV plants and grid–connected solar projects, as well as ensuring the viability and longevity of solar projects.

Additionally, we will determine the optimal inclination and orientation of solar modules based on the collected data. The model used in this study considers clear–sky index values and the probability density of fluctuations within the range of [0.0,0.9]. The fluctuations of the increments fall within the range of [-1,1], with a density of clear–sky index increments between [0.0,0.9], as estimated theoretically (Mucomole *et al.*, 2023; Duffie & Beckman, 1991). These findings can be extrapolated to other regions of interest using analogy. Through this research, we aim to provide updated tools for the optimal design and implementation of solar energy projects.

MATERIALS AND METHODS

Data Collection and Processing

The GHI data sample was obtained during the Mozambique solar radiation measurement campaign in the years 2012,2013 and 2014. The data was collected along the eastern–channel of Mozambique, specifically in the provinces of Maputo–city, Maputo–province, Gaza, Inhambane, Sofala, Manica, and Tete. Various stations were used to collect the data, including one in Maputo–city, one in Maputo–province, two in Gaza (Gaza–1 and Gaza–2), one in Inhambane, one in Sofala, one in Tete, and two in Manica (referred to as Manica–1 and Manica–2). A total of nine high–resolution radiometers, as shown in Figure 1, were utilized for this purpose.

Instrument and Sample Size

The GHI and Diffuse Horizontal Irradiation (DHI) components were collected using pyranometer sensors. These measurements were carried out in conjunction with a Pyrheliometer–integrated system, which allowed for the direct estimation of the component Direct Normal Irradiation (DNI).

Figure 1: Pyranometer used to measure GHI during the campaign

Data Selection

The data went through a comprehensive quality control procedure, removing any false values. Afterwards, dedicated software programs for radiation calculation were employed to analyze the data every 1 and 10 minutes. The purpose of preparing the sample was to perform calculations using data collected during the time period from sunrise to sunset (6:00 AM to 6:00 PM). The sample was obtained during the Mozambique campaign in various locations, namely Maputo–1, Maputo–2, Gaza–1, Gaza–2, Inhambane–1, Sofala–1, Manica–1, Manica–2, and Tete–1. The sample comprises three years of complete measurement data from 2012,2013 and 2014. The measurements commenced in the sixth month of each year, resulting in data covering only the months of June to December. However, in 2013 and 2014, the data includes measurements for all months of the year. In total, there are approximately 466.560,00 annually radiation data points collected in the designated area.

Figure 2, illustrates the range of the analyzed sample, specifically the Gaza–1 station, which demonstrates the highest count of satisfactory days, indicating excellent radiation levels, and accurate measurements obtained at the station, minimal interference from atmospheric factors, and other favorable conditions.

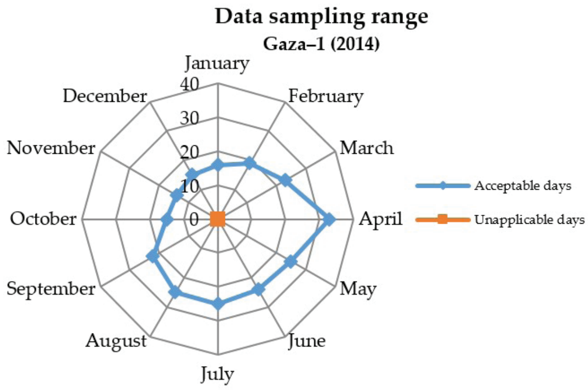

Figure 2: Range of global solar radiation data sample during the campaign (example from Gaza–1 station in 2014)

Certain months display fluctuations, which may include intervals or portions with incomplete data values, necessitating a pre–established categorization.

Study Area

Table 1, provides a comprehensive overview of the stations that have been established in the study area, which is the eastern region of Mozambique known as the channel region. The table includes various details such as the station number, station name, province, tower property and code station. The study area is situated between the 11°31°(-40)°E and 15°68'37"S parallels and meridian. The stations considered in this study comprise Maputo–1, Gaza–1, Gaza–2, Inhambane–1, Sofala–1, Manica–1, Manica–2, and Tete–1. Here Gaza–3 was disqualified due to the incompatible pattern and missing so much data.

Table 1: Location of study stations

Number	Station	Province	Tower property	Code
01	Maputo–1 – 01	Maputo–city	UEM	DF 01
02	Gaza–1 –02	Gaza	TDM	TDM
03	Gaza–2 – 03	Gaza	MCeL	TDM
04	Inhambane–1 – 04	Inhambane	MCeL	MCeL 11

05	Sofala–1 – 05	Sofala	FUNAE	TM11
06	Manica–1 – 06	Manica	MCeL	MCeL 14
07	Manica–2 – 07	Manica	MCeL	MCeL 14
08	Tete–1 – 08	Tete	FUNAE	TM6

In this context, MZ–Mozambique, UEM–Eduardo Mondlane University, DF–Department of Physics, TDM–Telecommunications of Mozambique, MC–Mozambique Cellphone, and TM–Mozambique Television.

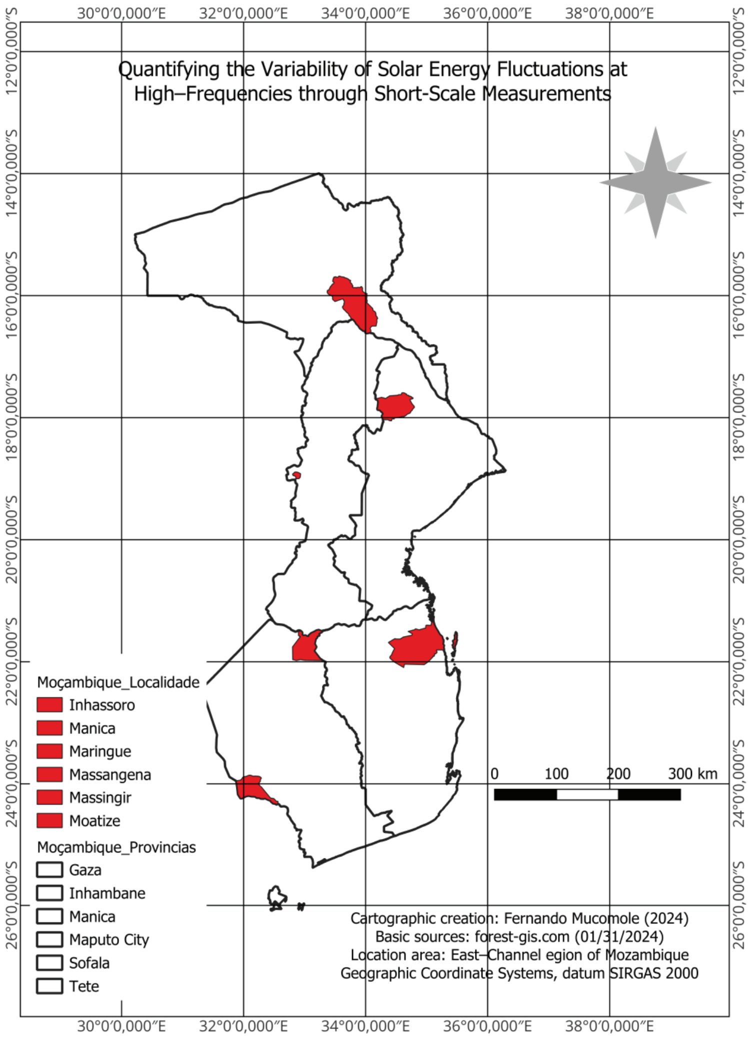

Figure 3: Study area: eastern–channel region of Mozambique

Figure 3, displays the topographic section of the east–channel region, showcasing the measuring stations.

METHODOLOGY

The analysis focused on the variable chronological time H, which ranges from 0 to 24 hours (standardized in degrees). In the morning, the hour angle w_s is less than 0, at noon it is equal to 0, and in the afternoon, it is greater than 0. This relationship is represented by equation 1 (eq.1) (Mucomole *et al.*, 2023).

$$\omega_s=(H-12)\times 15 \qquad \text{(eq. 1)}$$

The determination of the respective zenith angle θ_Z is enabled by the inverse of eq. 2 (Duffie & Beckman, 1991).

$$\theta_Z=(\mathrm{Cos}\,(\phi)\ \mathrm{Cos}\,(\delta)\ \mathrm{Cos}\,(\omega_s)\ +\mathrm{Sin}\,(\phi)\ \mathrm{Sin}\,(\delta)) \qquad \text{(eq. 2)}$$

In eq. 2, ϕ represents the declination. As depicted in Figure 4, it is evident that the θ_Z reaches its minimum value at noon, while it attains its maximum values during sunrise and sunset.

The calculation of extraterrestrial radiation G_0 involves determining the incident energy within a one–hour timeframe, using the solar constant in horizontal surface approximation provided in Duffie & Beckam (1991) as.

$$G_0=G_{on}=G_{sc}\,(1+0.033\mathrm{Cos}\ 360n/365\ )\mathrm{Cos}\ \theta_z \qquad \text{(eq. 3)}$$

Figure 5 illustrates the fluctuation of extraterrestrial radiation, showcasing its highest point during midday and its lowest points at sunrise and sunset.

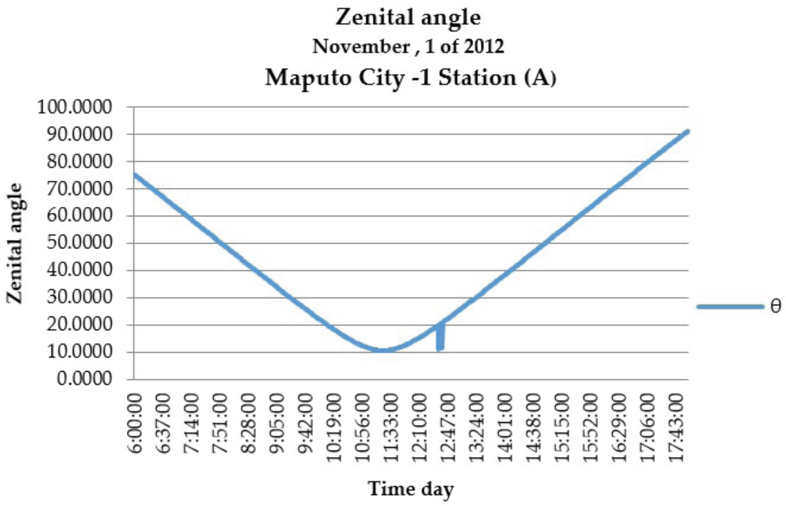

Figure 4: Zenithal angle (Maputo–city station: Year 2012)

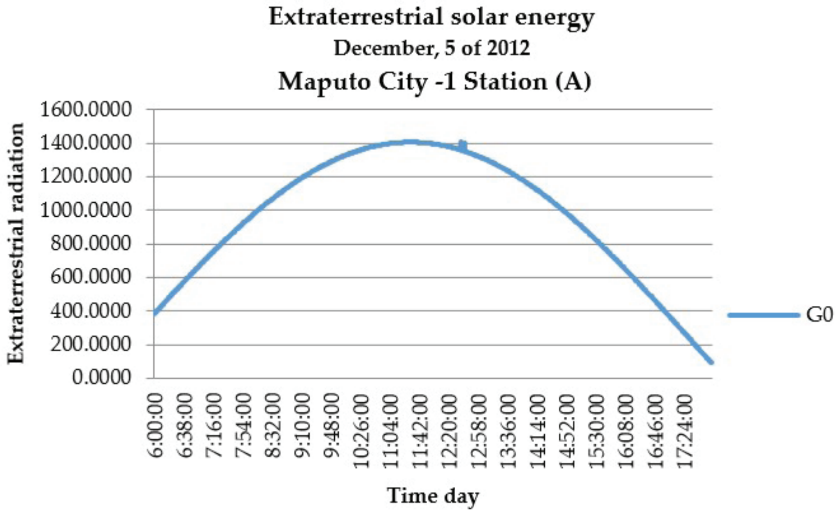

Figure 5: Examination of extraterrestrial radiation patterns (Maputo–city station: Year 2012)

The K^*_t can be defined as the ratio between the global horizontal irradiance (GHI) and the clear–sky radiation (Hoff & Perez, 2010; Mucomole *et al.*, 2023; R. Perez *et al.*, 2016; G. Lohmann, 2018), which represents the irradiation from the earth's atmosphere under clear–sky conditions (G. M. Lohmann & Monahan, 2018; Woyte *et al.*, 2007). It is worth noting that this index typically ranges from 0 to 1.0, providing a reliable estimate (R. Perez, David *et al.*, 2016; Mucomole *et al.*, 2023).

$K^*_t = GHI/G_{Clear}$ (eq. 4)

The total radiation on the horizontal surface, denoted as G_{Clear} or Total, represents the combined value of the direct radiation on the horizontal surface received within an and the diffuse radiation on the horizontal surface (Luoma *et al.*, 2011).

In order to assess the temporal analysis of temporal fluctuations (Lave *et al.*, 2012), a metric was employed to gauge the disparity between the successive and preceding clear–sky indices (Leung, 1980; Quoc Hung & Mishra, 2019). To ensure accurate findings, a precision interval was implemented to distinguish the variation between two consecutive measurements taken one minute apart as depicted in Figure 6.

The days were classified and organized based on the clear–sky index, as illustrated in Table 2 for the Gaza–2 station in 2012. The same procedure was followed for the rest of the sample across all stations.

Considering that the time period for measuring solar radiation on a flat surface is one day, as stated by Duffie & Beckam (1991), we can express this as follows,

$\Delta K^*_t = K^*_{(t+1)} - K^*_t$ (eq. 5)

The nominal variability refers to the variability of the dimensional clear–sky index, where the ramp rate ΔK^*_t is used as a scalable measure, as stated in Lohlman *et al.* (2018).

Nominal Variability $= \sqrt{(var[\Delta K^*_{t\Delta t}])}$ (eq. 6)

The eq. 7, will be utilized to calculate the sample standard deviation of N counts accumulation, considering a given irradiance of C=1000W/m^2 under standard conditions.

$$\sigma^{K^*_t} = \sqrt{\frac{1}{N-1}\sum_{t=1}^{M}\left(K^*_t(t) - \overline{K^*_t}\right)^2} \quad \text{(eq. 7)}$$

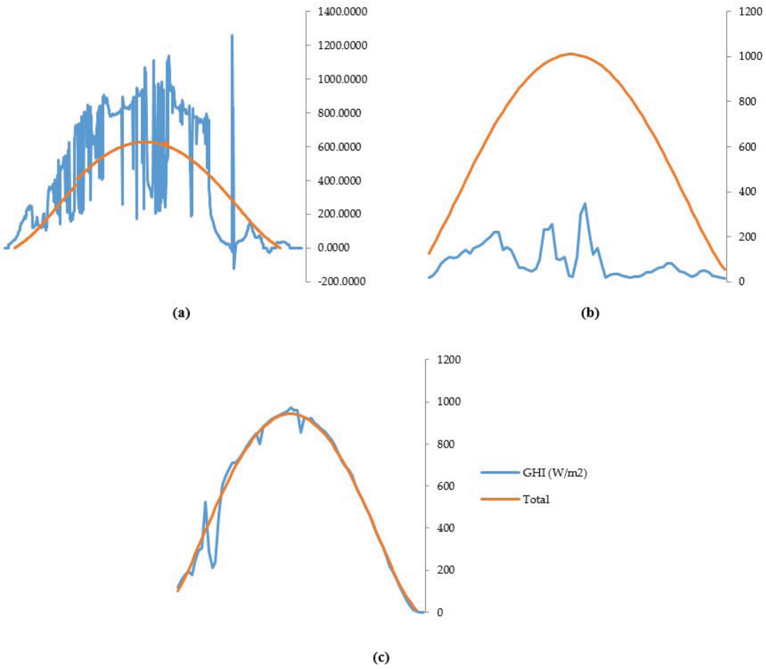

Figure 6: The contrast between experimental radiation and theoretical radiation is being examined

Table 2: Quantification of days types classification

Classification				
Mouth	**Clear**	**Cloudy**	**Low Intermediate**	**Upper Intermediate**
April	2	6	2	0
May	0	5	3	2
June	2	3	3	2
July	5	1	1	3
August	3	0	3	4
Setembro	2	2	2	4
October	1	3	2	4
November	7	0	1	2
December	0	4	5	1
Total	**22**	**24**	**22**	**22**

The correlation coefficient of the clear–sky index $\chi^{K^*t}_{ij}$ has been found to have a relationship with the distance for systematic connection across various types of days, including clear, intermediate, and cloudy. This relationship was determined using eq. 8 (R. Perez *et al.*, 2016).

$$\chi_{ij}^{k_t^*} = \frac{cov\left(K_{t,i}^*(t), K_{t,j}^*\right)}{\sigma_{K_{t,i}^*(t)}\sigma_{K_{t,j}^*}} \qquad \text{(eq. 8)}$$

The statistical value of $\chi^{K^*t}_{ij}$ falls within the range of -1 to 1, inclusive, encompassing values that are greater than or equal to -1 and less than or equal to 1 (Hoff & Perez, 2010).

Spatially, when considering a subspace station located between two points x and y, the randomized values that are associated with x+y can be calculated using the eq. 9 (Zheng *et al.*, 2023; Siebentritt, 2011; G. Lohmann, 2018)

$$\sigma_{x+y} = \sqrt{\sigma_x^2 + \sigma_y^2 + 2\rho_{xy}\sigma_x\sigma_y} \qquad \text{(eq. 9)}$$

It is important to note that $\sigma_{(K^*(t,i)(t))} \neq 0$ is not equal to zero and $\sigma_{(K^*(t,j))} \neq 0$ is also not equal to zero (Zhou *et al.*, 2019; G. Lohmann, 2018). The significance and changes of the average area's variability, based on the average area A, $\sigma^{(\Delta K^*t)}_{A}$, were determined through the utilization of random circle sampling in the southern and mid regions of the east–channel of Mozambique. This assessment was carried out using eq. 10 (R. Perez *et al.*, 2016; Hoff & Perez, 2010).

$$\hat{\sigma}_{STD}^{K_t^*} = \frac{\sigma_A^{K_t^*}}{\sigma_0^{K_t^*}} \qquad \text{(eq. 10)}$$

The normalized values of the average area quantities' variability $\sigma^{(\Delta K^*t)}_{STD}$, in relation to the standard deviation, were employed to evaluate its significance and any alterations.

RESULTS AND DISCUSSIONS

Categorization of Different Types of Days

The final classification of sky types (clear, intermediate, and cloudy) in the east–channel region of Mozambique varies in different years due to various factors that disrupt and diminish solar energy when it reaches the earth's surface. These variations in GHI are reflected in the quantities observed in the south region (Figure 7) and the mid region (Figure 8) in the east–channel.

The data presented in Figure 7 illustrates the classification of acceptable days for the years 2012,2013,and 2014. It reveals that the south region experienced the highest number of clear–sky days. Specifically, Maputo–1 had approximately 15 clear–sky days, Gaza–1 had around 23, and Gaza–2 had about 23 as well. Inhambane–1 recorded approximately 34 clear–sky days, while Tete–1 in the mid region had around 15.9 clear–sky days.

On the other hand, the south region also had a greater number of cloudy–sky days. Maputo–1 experienced around 14 cloudy–sky days, Gaza–1 had approximately 22, and Gaza–2 had around 23. Inhambane–1 recorded about 26 cloudy–sky days, while Tete–1 in the mid region had around 15 cloudy–sky days. Sofala–1 had 11 cloudy–sky days, Manica–1 had around 16, and Manica–2 had approximately 21.

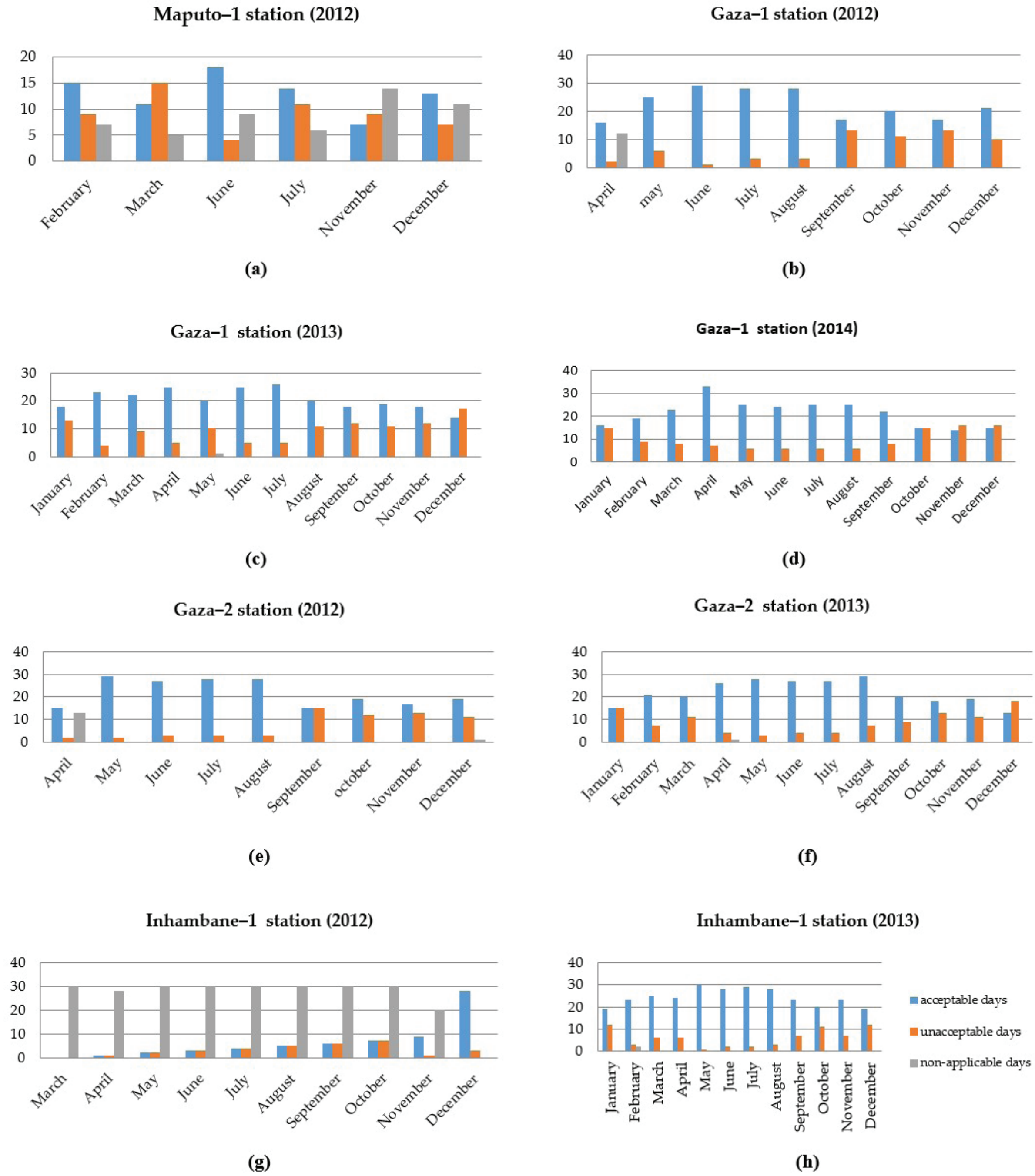

Figure 7: Displays the number of acceptable, unacceptable, and non-applicable days in the south region stations for various years. Specifically for: (a) Maputo–1 in 2012, Gaza–1 station (b) in 2012, (c) in 2013, (d) in 2014, Gaza–2 station (e) in 2012, (f) in 2013, Inhambane–1 station (g) in 2012 (h) in 2013

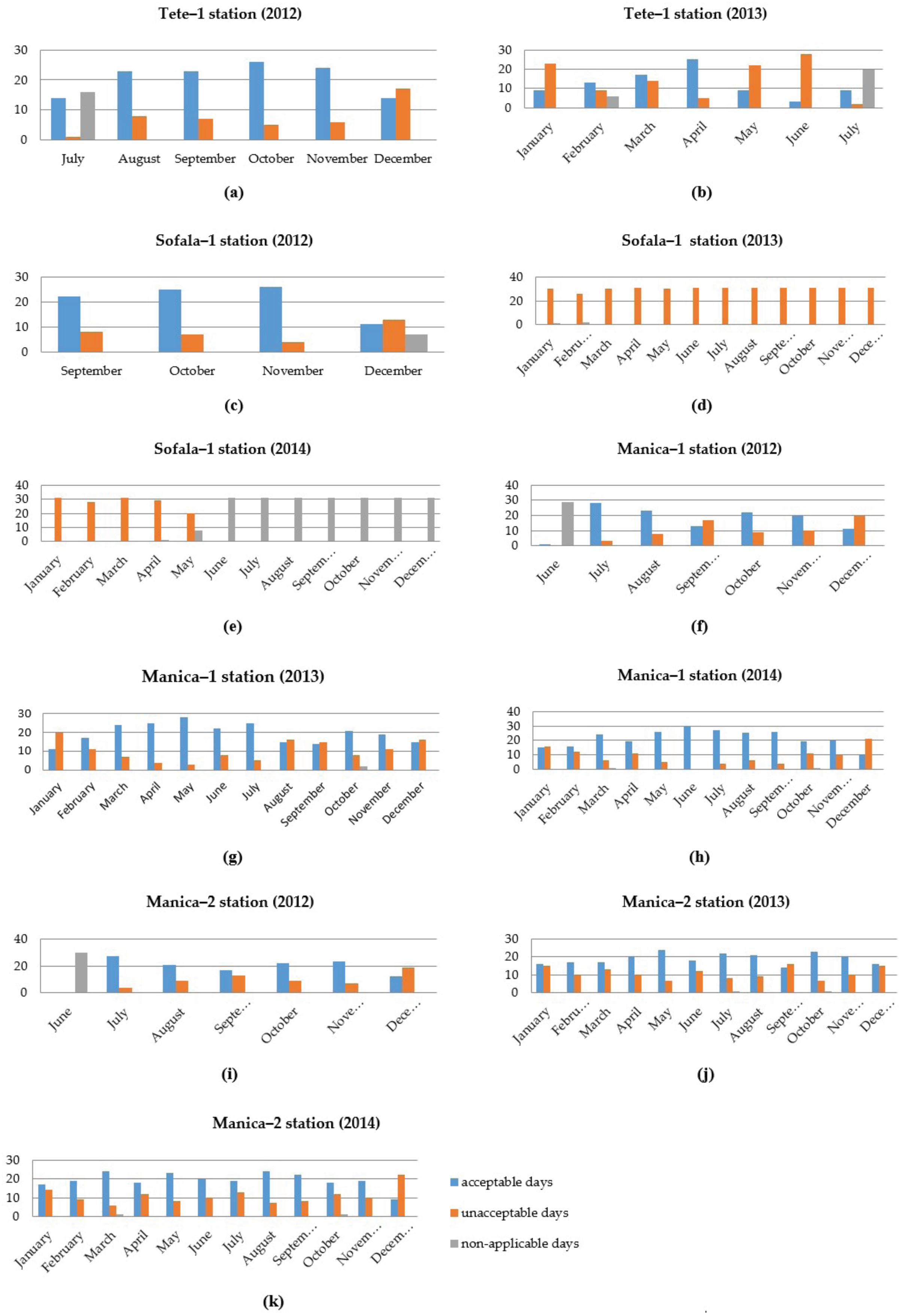

Figure 8: Number of acceptable, unacceptable, and non-applicable days in the mid region: Tete–1 station: (a) 2012, (b) 2013 , Sofala–1 station: (c) 2012, (d) 2013, (e) 2014, Manica–1 station: (f) 2012, (g) 2013, (h) 2014 and Manica–2 station: (i) 2012, (j) 2013, (k) 2014

In terms of intermediate–sky days, the mid region had the largest number. Tete–1 recorded around 30 days with both lower and upper intermediate–sky conditions, while Sofala–1 had 11 such days. Manica–1 had 28 days with lower intermediate–sky conditions and 59 days with upper intermediate–sky conditions. Manica–2 had 30 days with lower intermediate–sky conditions and 59 days with upper intermediate–sky conditions. In contrast, the south region had a smaller amount of intermediate–sky days. Maputo–1 had 28 days with lower intermediate–sky conditions, Gaza–1 had 45 days, and Gaza–2 had 44 days. Inhambane–1 recorded 58 days with lower intermediate–sky conditions.

In contrast, Figure 8 illustrates the distribution of unacceptable days in the years 2012,2013,and 2014. I reveals that the south region experienced a higher number of clear–sky days, with Maputo–1 having approximately 13 such days, Gaza–1 and Gaza–2 having around 13,25,and 24 days respectively, and Inhambane–1 having approximately 17,17 days. On the other hand, the mid region had a smaller number of clear–sky days, with Tete–1 having around 15 and 9 days, Sofala–1 having around 7, 26, and 26 days, and Manica–1 and Manica–2 having around 12,22,and 27 days, and 12,28,and 26 days respectively.

Furthermore, the south region experienced a greater number of cloudy–sky days, with Maputo–1 having around 20 days, Gaza–1 having around 13,25,and 32 days, and Gaza–2 having around 23 and 30 days. In contrast, the mid region had a smaller number of cloudy–sky days, with Tete–1 having around 15 and 14 days, Sofala–1 having around 8, 29, and 29 days, and Manica–1 and Manica–2 having around 12,25, and 29 days, and 12, 22 and 24 days respectively.

Moreover, the mid region had a greater number of intermediate–sky days (lower and upper), with Tete–1 having around 31 (17 and 14) days, 28 (15 and 13) days, Sofala–1 having around 8,29 and 29 days, and Manica–1 and Manica–2 having around 23 (12 and 11) days, 49 (25 and 24) days, 38 (24 and 14) days, and 24 (13 and 11) days, 47 (25 and 22) days, 55 (23 and 32) days respectively. Conversely, the south region had a smaller number of intermediate–sky days, with Maputo–1 having around 28 (4 and 14) days, Gaza–1 having around 26 (13 and 13) days, 48 (24 and 24) days, 47 (23 and 24) days.

Variations in the Clear–Sky Index and its Increments

Figure 9(a) Illustrates the Maputo–1 station, displaying the occurrence of K^*_t fluctuations in March between the range of [0.2252,1.0008], with the highest σK^*_t observed in November between the range of [0.0013,0.503]. On the other hand, Figure 10(a) exhibits high–frequencies of fluctuations in ΔK^*_t during March, ranging from [-0.0006,0.0907], with the highest trend σK^*_t occurring in July between the range of [-0.1751,1.0005]. The average PDF is estimated to be 0.04585, within the range of [0.0002,1.0007].

Figure 9(b) in the Gaza–1 station displays high–frequencies of K^*_t fluctuations in June 2012 ranging from [0.0834,1.0052], with a higher σK^*_t in May ranging from [0.0642,0.3523]. On the other hand, Figure 10(b) shows high–frequencies of ΔK^*_t fluctuations in December, ranging from [-0.7165,0.0033], with a higher trend σK^*_t in May ranging from [0.0511,0.7422]. The average PDF is estimated to be 0.1896, ranging from [0.0003,1.0001]. Moving on to 2013, Figure 9(c) illustrates high–frequencies of K^*_t fluctuations in June ranging from [0.1012,1.0022], with a higher σK^*_t in May ranging from [0.0553,0.8053]. Conversely, Figure 10(c) shows high–frequencies of ΔK^*_t fluctuations in January ranging from [-0.7341,0.0063], with the highest trend σK^*_t in May ranging from [0.0376,0.8053]. The average PDF is estimated to be 0.1285, ranging from [0.0001,0.8431]. In 2014, Figure 9(d) exhibits high–frequencies of K^*_t fluctuations in June ranging from [0.0937,1.0000], with the highest σK^*_t in December ranging from [0.0314,0.377]. Additionally, Figure 10(d) shows high–frequencies of ΔK^*_t fluctuations in December ranging from [-0.6353,0.6343], with a greater tendency σK^*_t in July ranging from [0.0294,0.996]. The average PDF is estimated to be 0.1439, ranging from [0.0021,1.0000].

Figure 9(e) in the Gaza–2 station displays the occurrence of high–frequencies of K^*_t fluctuations in April, ranging between [-1.0076,1.0076], with the highest σK^*_t observed in November, ranging between [0.0611,0.9804]. On the other hand, Figure 10(e) exhibits high–frequencies of ΔK^*_t fluctuations in August, ranging between [-1.0009,0.2523], with a greater tendency $\sigma \Delta K^*_t$ observed in November, ranging between [0.05044,0.8114].

The average PDF is estimated to be 0.1439, ranging between [0.0001,1.0017]. Moving on to 2013, Figure 9(f) illustrates high–frequencies of K^*_t fluctuations in August, ranging between [0.0744,1.0004], with the highest σK^*_t observed in March, ranging between [0.0317,0.3424]. Similarly, Figure 10(f) shows high–frequencies of ΔK^*_t fluctuations in May, ranging between [-0.964,0.3042], with a greater tendency $\sigma \Delta K^*_t$ observed in June, ranging between [0.0168,0.7512]. The average PDF is estimated to be 0.1166, ranging between [0.0001,0.8898].

Figure 9(g) at the Inhambane–1 station illustrates the occurrence of significant K^*_t fluctuations in January 2013, ranging from [0.0688,0.9973], with the highest σK^*_t observed in March within the range [0.0661,0.4644]. In Figure 10(g), there were notable fluctuations in ΔK^*_t during the month of July, ranging from [-0.5167,0.1666], with a higher trend $\sigma \Delta K^*_t$ observed in September within the range [0.0244,0.978]. The average PDF was estimated to be 0.1439, ranging from [0.0001,0.606]. In 2014, Figure 9(h) displays high–frequencies of K^*_t fluctuations in September, ranging from [0.0481,1.001], with the highest σK^*_t observed in December within the range [0.0235,0.4211]. In Figure 10(h), there were significant fluctuations in ΔK^*_t during the month of August, ranging from [-1.1001,0.0534], with a higher trend $\sigma \Delta K^*_t$ observed in July within the range [0.0204,0.6328]. The average PDF was estimated to be 0.12142, ranging from [0.0001,1.0036].

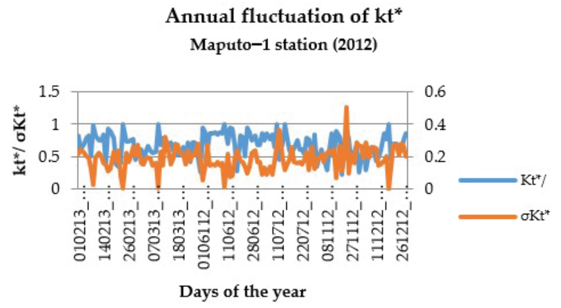

(a)

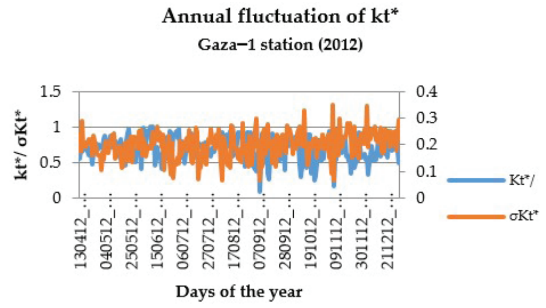

(b)

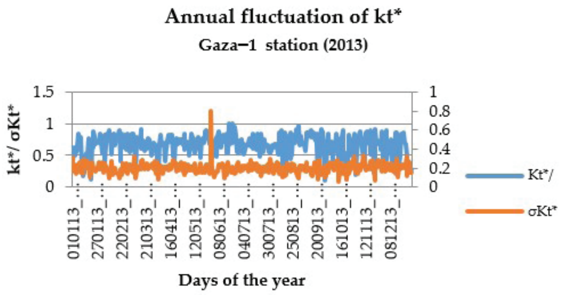

(c)

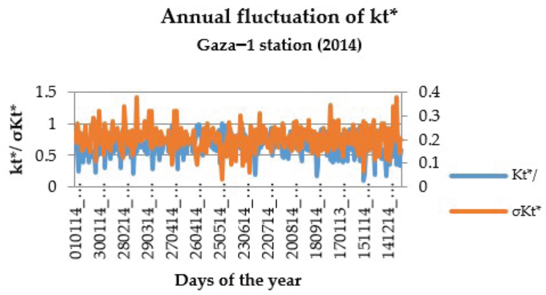

(d)

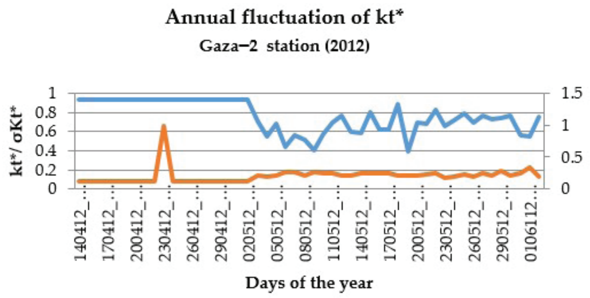

(e)

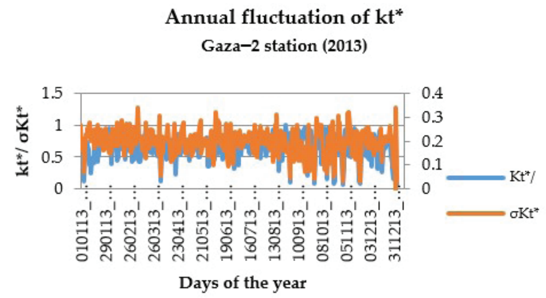

(f)

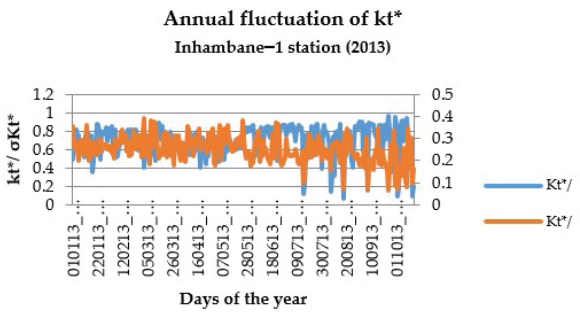

(g)

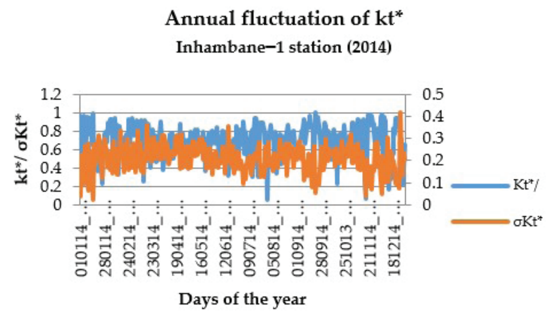

(h)

Figure 9: Annual fluctuations in clear–sky: Maputo–1 station: (a) in 2012, Gaza–1 station (b) in 2012, (c) in 2013, (d) in 2014, Gaza–2 station (e) in 2012, (f) in 2013, Inhambane–1 station (g) in 2012, (h) in 2013

In Figure 11, at the Tete–1 station, it can be observed that the year 2012 exhibits significant fluctuations in K^*_t frequencies during October, ranging between [0.2249,0.9892], with the highest σK^*_t occurring in July, ranging between [0.0204,0.3853]. On the other hand, Figure 12(a) illustrates high–frequencies of ΔK^*_t fluctuations in July, ranging between [-0.4479,0.0001], with a higher trend $\sigma\Delta K^*_t$ occurring in July, ranging between [0.0422,0.6091], and an average PDF of 0.0505, estimated between [0.0003,0.5788]. Moving on to 2013, Figure 11(b) displays high–frequencies of K^*_t fluctuations in February, ranging between [0.0001,0.9059], with the highest σK^*_t occurring in July, ranging between [0.001,0.3646]. However, in Figure 12(b), there were high–frequencies of ΔK^*_t fluctuations in January, ranging between [-0.957,0.7084], with a greater tendency $\sigma\Delta K^*_t$ occurring in April, ranging between [0.0001,0.648], and an average PDF of 0.054641, estimated between [0.0001,0.957].

At the Sofala–1 station, Figure 11(c) illustrates that in September of the year 2012, there are significant fluctuations in K^*_t with frequencies ranging from

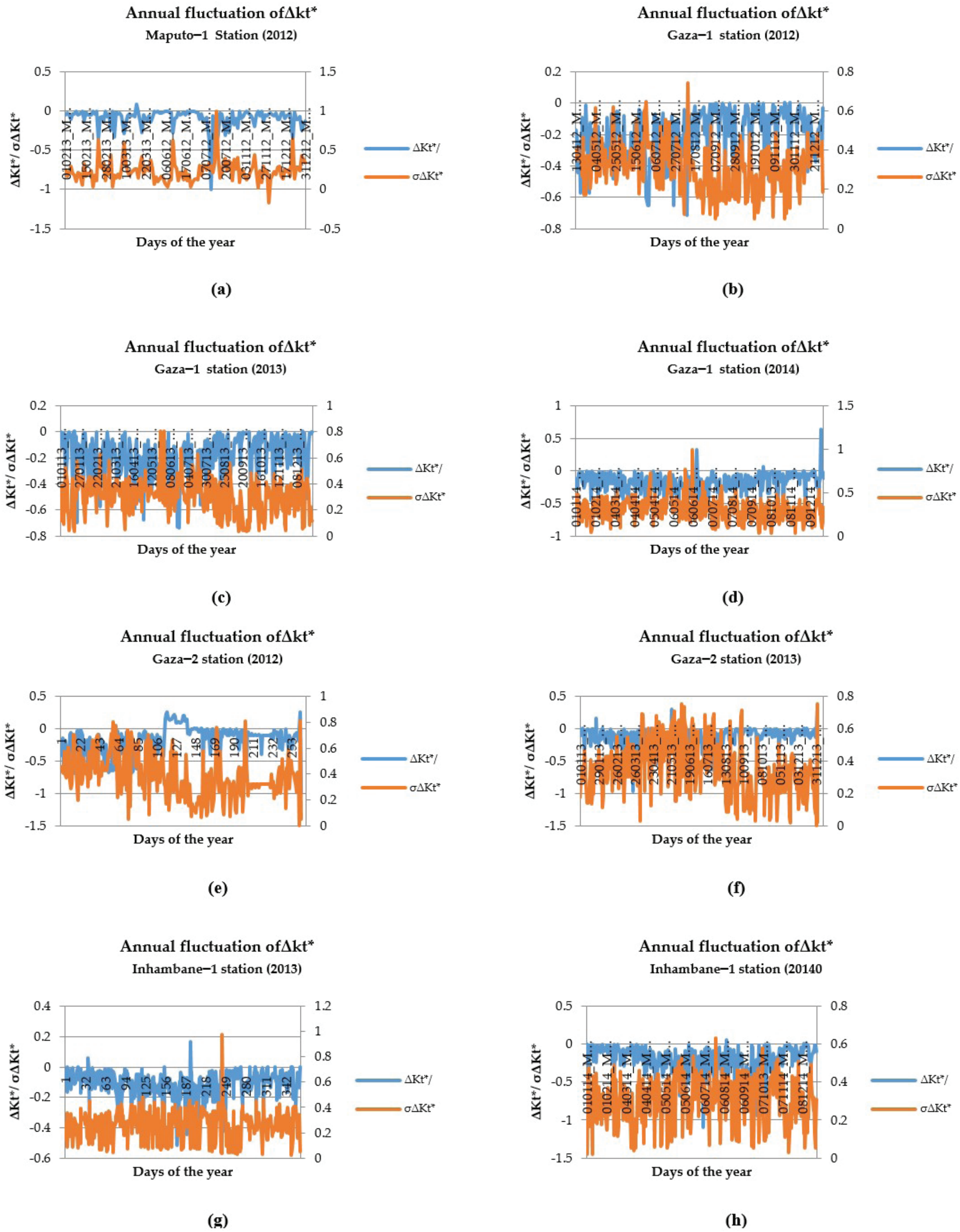

Figure 10: Fluctuations in clear–sky index increments: Maputo–1 station: (a) in 2012, Gaza–1 station: (b) in 2012, (c) in 2013, (d) in 2014, Gaza–2 station: (e) in 2012, (f) in 2013, Inhambane–1 station: (g) in 2013, (h) in 2014

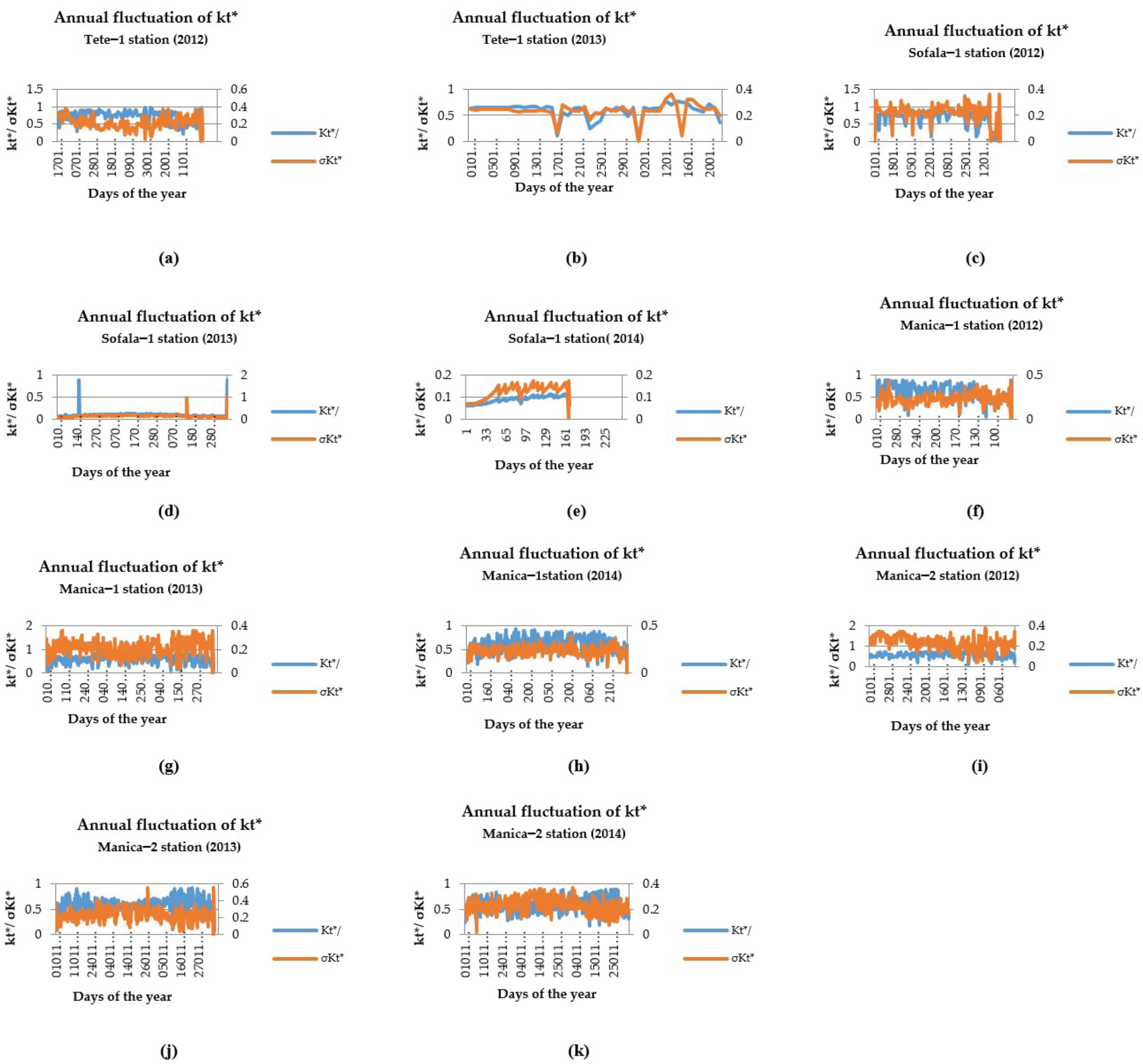

Figure 11: Annual fluctuations in clear–sky: Tete–1 station: (a) in 2012, (b) in 2013, Sofala–1 station: (c) in 2012, (d) in 2013, (e) in 2014, Manica–1 station: (f) in 2012, (g) in 2013, (h) in 2014, Manica–2 station: (i) in 2012, (j) in 2013, (k) in 2014

[0.0001,0.9688]. The highest σK^*_t is observed in December, with values between [0.0204,0.3853]. On the other hand, Figure 12(c) shows high–frequencies of ΔK^*_t fluctuations in December, ranging from [0.0001,0.0001]. The highest trend $\sigma\Delta K^*_t$ is observed in December as well, with values between [0.0422,0.6091]. The average PDF is estimated to be 0.0505, ranging from [0.0003,0.5788].

Moving on to 2013, Figure 11(d) displays high–frequencies of K^*_t fluctuations in February, ranging from [0.0019,0.8864]. The higher σK^*_t is observed in October, ranging from [0.0465,0.99]. In contrast, Figure 12(d) shows high–frequencies of ΔK^*_t fluctuations in December, ranging from [-0.1131,0.0628]. The greater tendency $\sigma\Delta K^*_t$ is observed in November, ranging from [0.01007,0.792]. The average PDF is estimated to be 0.0457, ranging from [0.002,0.367].

Lastly, in 2014, Figure 11(e) presents high–frequencies of K^*_t fluctuations in December, ranging from [0.0613,0.1143]. The highest σK^*_t is observed in October, ranging from [0.0679,0.1737]. On the other hand, Figure 12(e) shows high–frequencies of ΔK^*_t fluctuations in September, ranging from [-0.0152,0.0049]. The higher trend $\sigma\Delta K^*_t$ is observed in October, ranging from [0.021,0.1445]. The average PDF is estimated to be 0.041827, ranging from [0.0128,0.0836].

Figure 11(f) at the Manica–1 station displays significant K^*_t fluctuations in June 2012, ranging from [0.0492,0.8943], with the highest σK^*_t occurring between [0.05596,0.4225]. On the other hand, Figure 12(f) shows notable fluctuations in ΔK^*_t during December, ranging from [-0.6607,0.0006], with a higher trend $\sigma\Delta K^*_t$ in June between [0.0405,0.776]. The average PDF is 0.05382, estimated between [0.005,0.845], for the year 2013. Moving on to Figure 11(g), it illustrates high–frequencies of K^*_t fluctuations in July 2013, ranging from [0.0734,0.9543], with higher σK^*_t in November between [0.0382,0.3592].

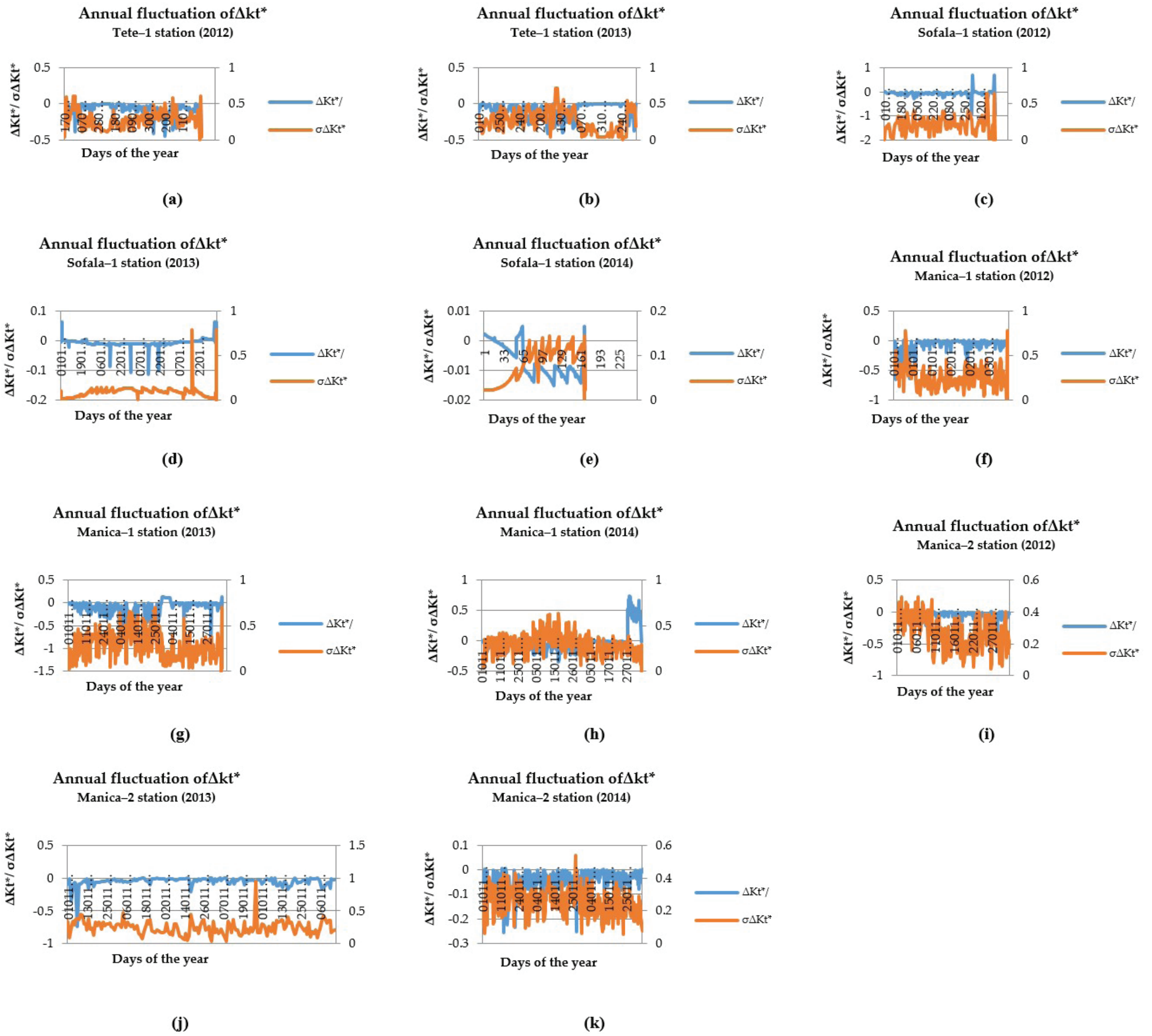

Figure 12: Fluctuations of clear–sky index and its increments: Tete–1 station: (a) in 2012, (b) in 2013, Sofala–1 station: (c) in 2012, (d) in 2013, (e) in 2014, Manica–1 station: (f) in 2012, (g) in 2013, (h) in 2014, Manica–2 station: (i) in 2012, (j) in 2013, (k) in 2014

Comparison of the Variation in Clear–Sky Index During the Years 2012, 2013, and 2014

Throughout the years examined, Figure 13(a) depicted that the Maputo–1 station exhibits the highest levels of radiation during the hot and rainy season, while the lowest levels of radiation occur during the cool and dry season. However, in 2012, there is a noticeable rise in the average K^*_t, reaching 0.6781. Figure 14(a) depicted that this increase is accompanied by a deviation trend of 0.1867 and a negative increment of -0.088 in the K^*_t, indicating a shift towards 0.3093. The PDF function estimates the K^*_t to be 0.0459 across all years.

Throughout the years season analyzed, Figure 13(b) illustrates that Gaza–1 exhibits contrasting weather patterns. The hot and rainy season consistently experiences the highest levels of radiation, while the cool and dry season consistently witnesses the lowest levels of radiation. However, an interesting trend emerges in the years 2012, 2013, and 2014, as there is a notable increase in the average radiation index during these years. The K^*_t, which measures the amount of radiation received under cloudless conditions, is recorded as 0.6979,0.6612,and 0.6667 respectively. There is a deviation trend towards 0.2014, indicating a slight increase in radiation levels. Additionally, Figure 14(b) shows that ΔK^*_t also shows an upward trend, with values of 0.3152,0.30925,and 0.3145 respectively. This further supports the deviation trend towards 0.3093. Interestingly, the PDF function estimates the radiation index to be 1.0001 in all years.

Throughout the years season analyzed, Figure 13(c) shows that Gaza–2 exhibits contrasting weather patterns. It experiences a hot and rainy season characterized by high levels of radiation, while the cool and dry season witnesses the lowest levels of radiation. However, in the years 2012 and 2013, there is a notable rise in the average K^*_t, measuring at 0.7595 and 0.6574 respectively.

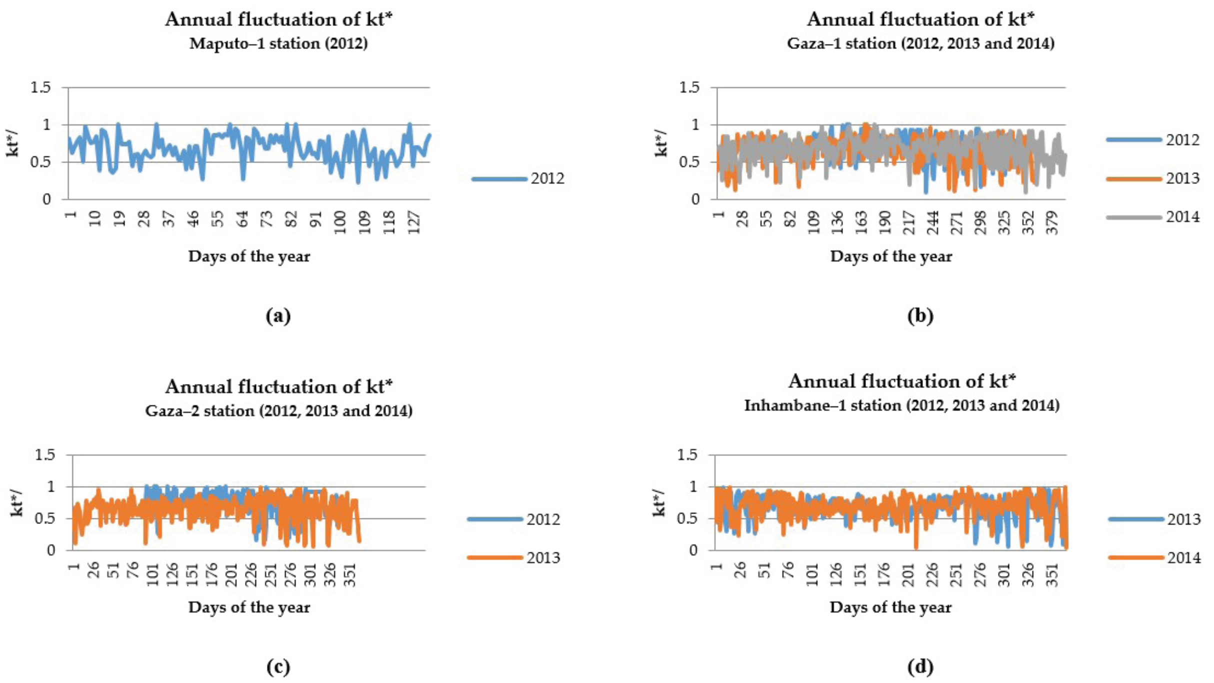

Figure 13: Fluctuations of clear–sky index: (a) Maputo–1 station (2012), (b) Gaza–1 station (2012, 2013, 2014), (c) Gaza–2 station (2012, 2013, 2014), (d) Inhambane–1 station (2012, 2013, 2014)

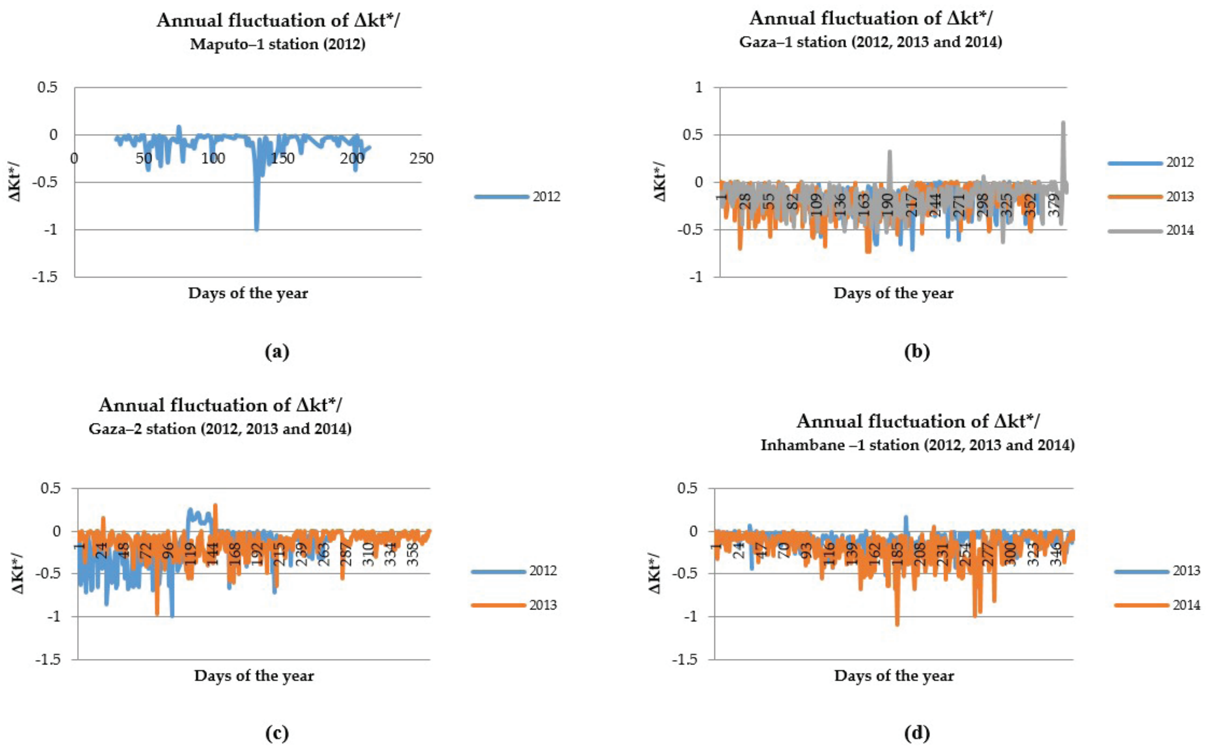

Figure 14: Fluctuations of clear sky–index increments: (a) Maputo–1 station (2012), (b) Gaza–1 station (2012, 2013, 2014), (c) Gaza–2 station (2012, 2013, 2014), (d) Inhambane–1 station (2012, 2013, 2014)

In Figure 14(c) shows that this increase is accompanied by a deviation trend towards 0.1959 and a rise in the ΔK^*_t of -0.1935 and -0.1367. Additionally, there is a deviation trend towards 0.3854. The PDF function estimates whether the 0.1957 is consistent across all years.

Throughout the years analyzed, Figure 13(d) depicted that Inhambane–1 station consistently exhibits the highest levels of radiation during the hot and rainy season, while the lowest levels of radiation are observed during the cool and dry season. However, in the years 2013 and 2014, there is a notable increase in the average K^*_t. Specifically, the K^*_t values for those years are 0.6962 and 0.7019, respectively. Additionally, there is a deviation trend towards 0.2454, indicating a shift from the average.

Moreover, Figure 14(d) shows that there is an increase in the ΔK^*_t of -0.1142 and -0.1979 for the respective years, along with a deviation trend towards 0.2982. The PDF function estimates whether the value of 0.1214 holds true for all years.

Throughout the years analyzed, Figure 15(a) depicted that Tete–1 station consistently exhibits the highest levels of radiation during the hot and rainy season, while the lowest levels of radiation are observed during the cool and dry season. However, in the years 2012 and 2013, there is a notable increase in the average K^*_t measuring 0.7131 and 0.5877 respectively. Figure 16(a) shows that this increase is accompanied by a deviation trend towards 0.2323 and an ΔK^*_t of -0.0785 and -0.0851 respectively. Additionally, there is a deviation trend towards 0.2839. The PDF function estimates a value of 0.0504 for all years.

Figure 15(b) depicted that Sofala–1 station, the hot and rainy season exhibits higher radiation levels, while the cool and dry season experiences lower radiation levels.

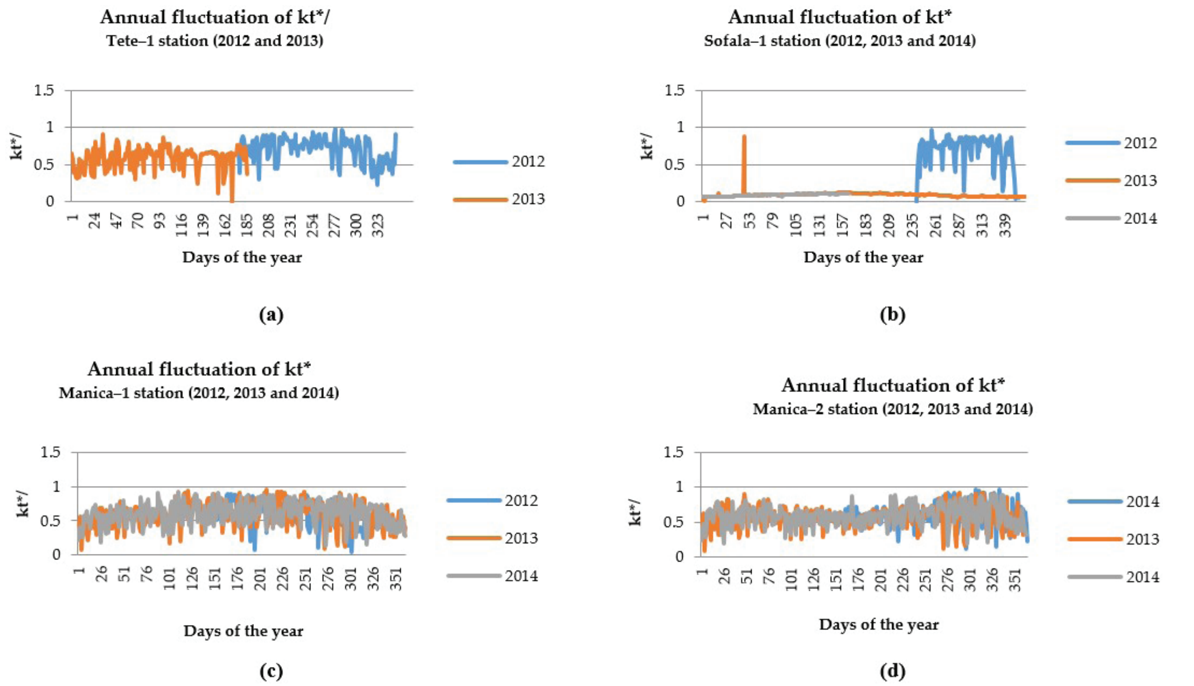

Figure 15: Annual fluctuations of clear sky–index: (a) Tete–1 station (2012, 2013), (b) Sofala–1 station (2012, 2013, 2014), (c) Manica–1 station (2012, 2013, 2014), (d) Manica–2 station (2012, 2013, 2014)

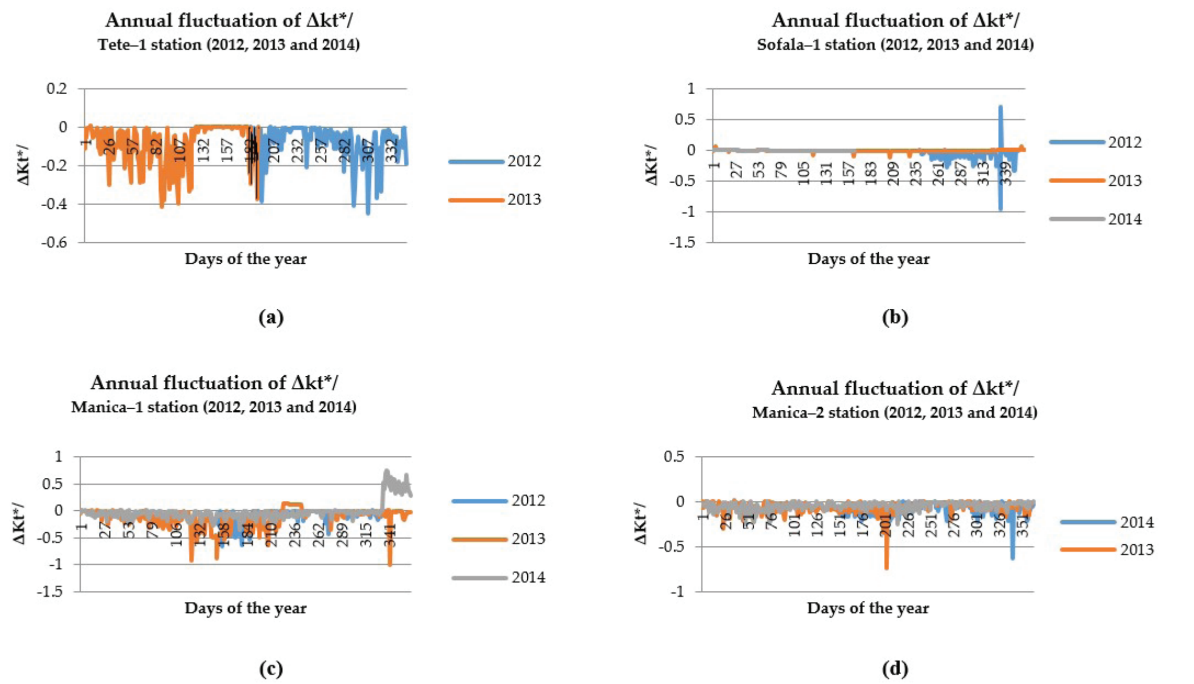

Figure 16: Annual fluctuations of clear–sky index increments: (a) Tete–1 station (2012, 2013), (b) Sofala–1 station (2012, 2013, 2014), (c) Manica–1 station (2012, 2013, 2014), (d) Manica–2 station (2012, 2013, 2014)

However, in the years 2012,2013 and 2014, there is a recorded increase in the average K^*_t. The values for these years are 0.6839,0.0902 and 0.0882 respectively. There is also a trend towards a deviation of 0.2205. Additionally, Figure 16(b) depicted that there is an increase in the ΔK^*_t, with values of -0.0761,-0.007 and -0.0069, and a deviation trend towards 0.2089. The PDF function estimates a value of 0.0547 for all years.

In other Figure 15(c) shows that Manica–1 station, the hot and rainy season exhibits higher radiation levels, while the cool and dry season experiences lower radiation levels. However, in the years 2012, 2013, and 2014, there is a noticeable rise in the averageK^*_t. Specifically, the K^*_t values for these years are recorded as 0.6154,0.6015 and 0.6042 respectively. Moreover, there is a trend towards deviation with a value of 0.2366.

Additionally, Figure 16(c) shows that the ΔK^*_t shows an increase of -0.0898,-0.1113 and -0.0182 for the respective years, with a deviation trend towards 0.3093. The PDF function estimates the K^*_t to be 0.1026 for all years.

Finally in Figure 15(d) its shows that in Manica–2 station, the hot and dry season exhibits higher radiation levels, while the cool and rainy season experiences lower radiation levels. However, in the years 2012,2013 and 2014, there is a noticeable rise in the average K^*_t. Specifically, the K^*_t values for these years are recorded as 0.6026,0.5823 and 0.5902 respectively. Moreover, there is a deviation trend towards 0.2322, indicating an increasing pattern. Additionally, Figure 16(d) depicted that the ΔK^*_t for these years is -0.0755,-0.0609 and -0.0484 respectively, with a deviation trend towards 0.3093. The PDF function estimates the K^*_t to be 0.03269 for all years.

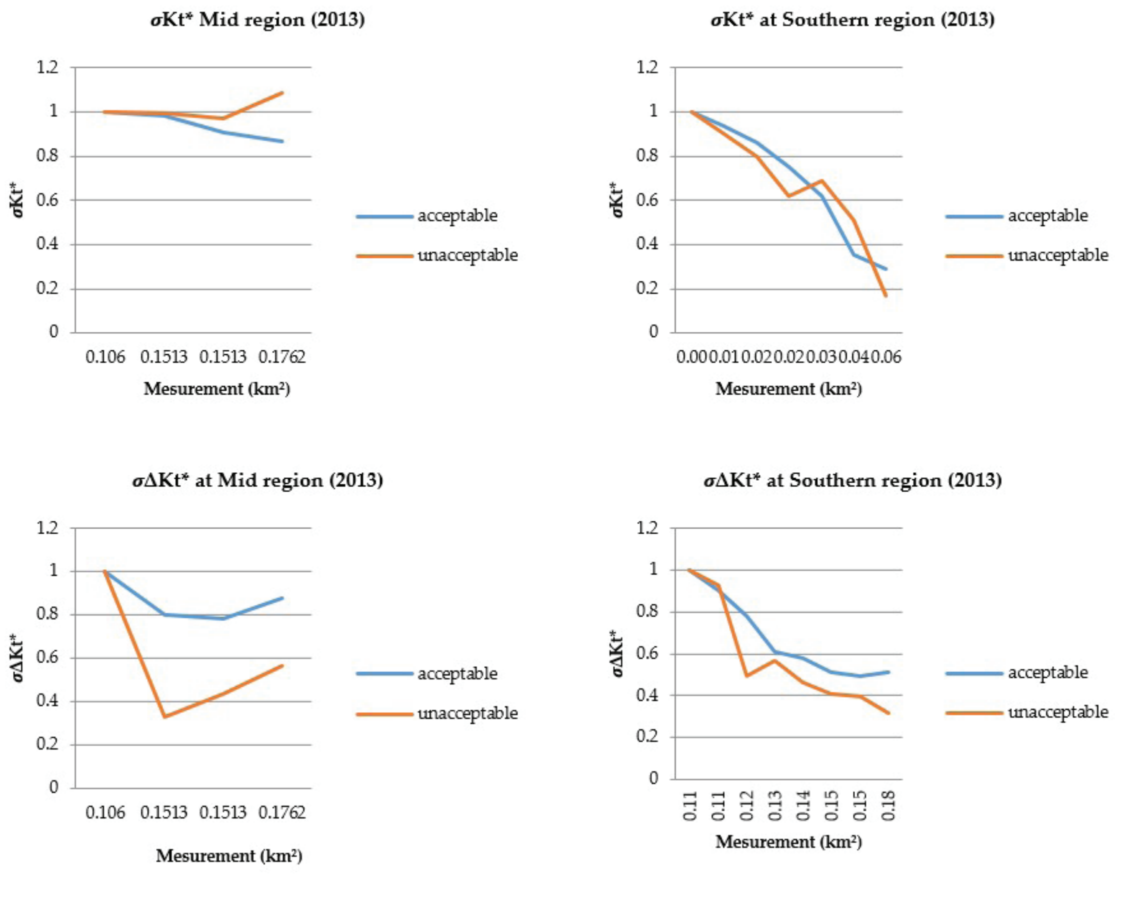

(a) (b)

Figure 17: The increments of normalized standard deviations for the area of the normalized clear–sky index in the: (a) Mid region and (b) Southern region

Evaluation of Standardized Fluctuation in the Eastern–Channel

The normalized values of the variability of average quantities in the area were assessed using the relative standard deviation. This assessment was conducted individually for each pyranometer positioned at the station, considering the sky type and subsequently all sky types.

After calculating the correlation measure between stations and evaluating the correlation coefficient, the comprehensive analysis depicted in Figures 17(a) and 17(b) revealed that the reduction in variability is more pronounced for shorter increment times when compared to longer increments, as indicated by the mean area.

Furthermore, the rate of decrease is not as fast for cloudy–sky conditions in comparison to other sky conditions. The decrease in ΔK^*_t was noted for both t=1 min and t=10 min. Nevertheless, apart from the 1 min intervals during cloudy–sky conditions mentioned previously, the scales at which the increments lose correlation are relatively small when compared to the ratio of the circular arenas utilized for computing averages area.

DISCUSSION

The annual K^*_t averages in the eastern–channel of Mozambique from 2012 to 2014 exhibit a varying trend towards decrease. The recorded values for K^*_t averages are as follows: 0.6979,0.6612 and 0.66677 at Gaza–1 station, 0.7597,and 0.6574 at Gaza–2 station, 0.6962,and 0.7019 at Inhambane–1 station, 0.7132 and 0.5877 at Tete–1 station, 0.6839,0.0902,and 0.0882 at Sofala–1 station, 0.6839,0.0902 and 0.0882 at Manica–1 station, 0.6026,0.5823 and 0.5902 at Manica–2 station, and 0.6782 at Maputo–1 station, with a deviation trend towards 0.1867. The primary reason behind this occurrence is pollution from extractive, commercial, and manufacturing industries, along with uncontrolled fires that emit harmful gases and particles into the atmosphere. These elements disrupt the hydrological cycle and prevent the transmission of solar radiation to the Earth's surface. Mucomole *et al.* (2023) have also noted a similar pattern in the southern region of Mozambique, where atmospheric conditions prevent solar radiation.

Various studies, such as those by Lave *et al.* (2012), Sha & Aiello (2018), Behr *et al.* (2021), Syed & Khalid (2021), and Elfeky *et al.* (2023), have discussed the fluctuations in K^*_t and the influence of geographic smoothing on reducing variability. Furthermore, Quoc Hung & Mishra (2019) have effectively minimized energy loss and enhanced the profile by addressing PV voltage fluctuations. Perpiñán *et al.* (2013) have achieved comparable outcomes, demonstrating that the relationship between intermediate time scales and daily fluctuation levels impacts the electrical energy fluctuations in PV inverters.

The annual mean values of ΔK^*_t in the east–channel region of Mozambique displayed temporal fluctuations during the years 2012,2013 and 2014. At the Gaza–1 station, the recorded values were 0.3152,0.3093 and 0.3145 respectively. Similarly, at the Gaza–2 station, the values were -0.1935,-0.1367 and -0.1142. The Inhambane–1 station registered values of -0.0785,-0.0851 and -0.1979. The Tete–1 station had values of -0.0761,-0.007 and -0.0069. The Sofala–1 station observed values of 0.0898,-0.1113 and -0.0182. The Manica–1 station recorded values of -0.0755,-0,0609 and -0.0484. The Manica–2 station had a value of -0.088. Lastly, the Maputo–1 station recorded a value of -0.088. On average, the deviation tendency was 0.3093, indicating the influence of various factors that disrupt the atmosphere and its cycle, resulting in rapid fluctuations in cloudiness and solar energy. This finding is consistent with the research conducted by Perpiñán & Lorenzo (2011), which reported similar outcomes regarding the impact of gases, solid particles, and cloud movements on PV generation. Tiba *et al.* (2016) also discovered that longer time intervals lead to greater variation in ramp rates. Additionally, G. Lohmann (2018) and G. M. Lohmann *et al.* (2016) observed significant changes in the distributions of increments from multiple pyranometers as time intervals increased. Another study by Kumar *et al.* (2022) optimized costs by evaluating ramp rates to mitigate the impact of increasing PV power on voltage fluctuations.

A faster decrease in variability is observed for shorter increment times when examining the spatial averages of deviation along the station circles, which are measured at interprovincial distances. Previous studies by Lohmann *et al.* (2018), Marcos *et al.* (2011), Hoff & Perez (2010), and Hoff & Perez (2011) have also reported similar findings, suggesting that the impact of longer decorrelation distances and higher spatial correlation coefficients is considerably more significant in a centralized PV plant compared to a distributed scenario.

CONCLUSIONS

The solar energy resource exhibits a remarkable level of availability despite the ongoing climate changes. This availability is characterized by fluctuations in solar energy, which can be quantified using the high–frequency clear–sky index. Throughout the study region, there is an observed increase in solar energy. However, it is crucial to comprehend the limited lifespan of PV projects, along with the temporal variability and spatial averaging that impact the functioning of PV systems and other related projects. By analyzing the sample of GHI, measured at nine stations located across the eastern–channel of Mozambique, we have reached the following conclusions:

1. To ensure the successful implementation of the model, it is important to consider the range of solar energy fluctuations, which typically vary between 0 and 1.0;
2. Days with intermediate–sky conditions pose a higher risk as they have a probability density value of approximately 1.0 and exhibit greater deviations in the clear–sky index. These conditions can potentially have a significant impact on the performance of a PV plant;
3. Clear and cloudy–sky days, on the other hand, show a lower tendency and deviation from the clear–sky index, with solar energy frequencies remaining relatively constant.
4. The decrease in variability is more pronounced for shorter time increments (1 min) compared to longer increments (10 min). Additionally, the decrease is less rapid for cloudy–sky conditions compared to other sky types.
5. Both for time increments of 1 min and 10 min, the decrease in ΔK^*_t (decorrelation) is observed as interprovincial distances of thousands of kilometers are crossed.
6. Under cloudy–sky conditions, the decorrelation scales for increments are relatively small compared to the ratio of the circles used to calculate area averages. These scales are estimated to be in the range of thousands of kilometers for interprovincial distances.
7. When planning a PV plant, it is crucial to consider fluctuations in order to prevent the output power of

the plant from being compromised. It is observed that longer decorrelation distances, resulting in higher spatial correlation coefficients, have a stronger impact on centralized PV plants compared to scenarios where the PV units are more distributed within the same plant.

In the eastern–channel of Mozambique, there are significant variations in solar energy levels during the hot and rainy season, particularly in December. This is characterized by high–frequency densities of solar energy fluctuations. The observations from various stations in the region are as follows: at the Maputo–1 station, the observed magnitude was 1.0 in 2012; at the Gaza–1 station, the observed magnitudes were 1.0001 in 2012 and 2014, and 0.8431 in 2013; at the Gaza–2 station, the observed magnitudes were 1.0017 in 2012 and 0.8898 in 2013; at the Inhambane–1 station, the observed magnitudes were 0.6060 in 2012 and 1.0036 in 2013; at the Sofala–1 station, the observed magnitudes were 0.9570 in 2012, 0.3670 in 2013, and 0.0836 in 2014; in Manica–1 station, the observed magnitudes were 0.8450 in 2012, 1.0002 in 2013, and 0.8314 in 2014; at the Manica–1 station, the observed magnitudes were 0.2367 in 2012, 0.4020 in 2013, and 0.1879 in 2014; at the Tete–1 station, the observed magnitudes were 0.5788 in 2012 and 0.3486 in 2014. On the other hand, during the cold and dry season, the densities of low–frequency solar energy are lower, particularly in June. This season is characterized by a greater occurrence of cloudy–sky days. The observed magnitudes from different stations during this season are as follows: at the Maputo–1 station, the observed magnitude was 0.0002 in 2012.

At the Gaza–1 station, the observed magnitudes were 0.0003 in 2012, 0.0001 in 2013, and 0.0028 in 2014; at the Gaza–2 station, the observed magnitudes were 0.0001 in 2012,2013,and 2014; at the Inhambane–1 station, the observed magnitudes were 0.0001; similarly, at the Sofala–1 station, the measurements were 0.0001 in 2013 and 2014; at the Manica–1 station, the measurements were 0.0001 in 2012, 0.0002 in 2013, and 0.0012 in 2014; the Manica–2 station recorded measurements of 0.0050 in 2012, 0.0031 in 2013, and 0.0058 in 2014; at the Tete–1 station, the measurements were 0.0026 in 2012, 0.0241 in 2013, and 0.0074 in 2014; finally, at the Tete–1 station, the measurements were 0.0003 in both 2012 and 2013.

Future Tasks

In addition to employing the aforementioned normal distribution method to evaluate the variability of the clear–sky index using a probability density function derived from data gathered from nine GHI stations, it is crucial to investigate the utilization of the standard normal distribution in relation to cloud data. This includes examining factors such as speed and/or position, which are measured on a smaller scale. This approach would contribute to a better understanding of sudden changes in solar energy at the earth's surface, ultimately enhancing the effectiveness of PV projects and other solar energy applications.

Source of Funding

This research is funded by CS–OGET (Center of Excellence of Studies in Oil and Gas Engineering and Technology), from the Faculty of Engineering of Eduardo Mondlane University.

Acknowledgments

The findings of this study are not yet published, but they can be obtained from INAM, FUNAE, UEM, or by contacting the corresponding author and making a reasonable request.

REFERENCES

Akuffo, F. O., & Brew-Hammond, A. (1993). The frequency distribution of daily global irradiation at Kumasi. *Solar Energy, 50*(2), 145–154. https://doi.org/10.1016/0038-092X(93)90086-4

Alam, M. J. E., Muttaqi, K. M., & Sutanto, D. (2014). A Novel Approach for Ramp-Rate Control of Solar PV Using Energy Storage to Mitigate Output Fluctuations Caused by Cloud Passing. *IEEE Transactions on Energy Conversion, 29*(2), 507–518. https://doi.org/10.1109/TEC.2014.2304951

Alva, G., Liu, L., Huang, X., & Fang, G. (2017). Thermal energy storage materials and systems for solar energy applications. *Renewable and Sustainable Energy Reviews, 68,* 693–706. https://doi.org/10.1016/j.rser.2016.10.021

Anvari, M., Lohmann, G., Wächter, M., Milan, P., Lorenz, E., Heinemann, D., Tabar, M. R. R., & Peinke, J. (2016). Short term fluctuations of wind and solar power systems. *New Journal of Physics, 18*(6), 063027. https://doi.org/10.1088/1367-2630/18/6/063027

Attaviriyanupap, P., Tokuhara, K., Itaya, N., Marmiroli, M., Tsukamoto, Y., & Kojima, Y. (2011). Estimation of photovoltaic power generation output based on solar irradiation and frequency classification. *2011 IEEE PES Innovative Smart Grid Technologies,* 1–7. https://doi.org/10.1109/ISGT-Asia.2011.6167078

Behr, H., Jung, C., Trentmann, J., & Schindler, D. (2021). Using satellite data for assessing spatiotemporal variability and complementarity of solar resources – a case study from Germany. Meteorologische Zeitschrift. https://doi.org/10.1127/metz/2021/1081

Cai, Y.-H., & Schäfer, A. I. (2020). Renewable energy powered membrane technology: Impact of solar irradiance fluctuation on direct osmotic backwash. *Journal of Membrane Science, 598,* 117666. https://doi.org/10.1016/j.memsci.2019.117666

Chen, W.-H., Cheng, L.-S., Chang, Z.-P., Zhou, H.-T., Yao, Q.-F., Peng, Z.-M., Fu, L.-Q., & Chen, Z.-X. (2022). Interval Prediction of Photovoltaic Power Using Improved NARX Network and Density Peak Clustering Based on Kernel Mahalanobis Distance. *Complexity, 2022,* 1–22. https://doi.org/10.1155/2022/8169510

Diaz, V. N. S. (2019). Avaliação de desempenho das estratégias de controle para suavização da potência ativa de sistemas fotovoltaicos com armazenamento de energia. https://tede.unioeste.br/handle/tede/4632

Domingos, S. F., Monteiro, L. G., & Boaventura, W. do C. (2020). Estado Da Arte Para Previsão Da Radiação Solar. Anais Congresso Brasileiro de Energia Solar - CBENS. https://doi.org/10.59627/cbens.2020.742

Duffie, J. A., & Beckman, W. A. (1991). Solar Engineering of Thermal Processes.

Elfeky, K. E., Mohammed, A. G., Ahmed, N., & Wang, Q. (2023). Thermal performance of cascaded and combined sensible-latent heat storage tank under fluctuations in sunlight and electric demand. *Applied Thermal Engineering, 229,* 120575. https://doi.org/10.1016/j.applthermaleng.2023.120575

Exell, R. H. B. (1976). The fluctuation of solar radiation in Thailand. *Solar Energy, 18*(6), 549–554. https://doi.org/10.1016/0038-092X(76)90074-8

Gomes, C. C. C., Torres, I. C., & Tiba, C. (2020). Taxas de rampas de irradiância e potência. *CIES2020 - XVII Congresso Ibérico e XIII Congresso Ibero-americano de Energia Solar,* 927–934. https://doi.org/10.34637/cies2020.1.6110

Gomes, J. M., Ferreira, P. M., & Ruano, A. E. (2011). Implementation of an intelligent sensor for measurement and prediction of solar radiation and atmospheric temperature. *2011 IEEE 7th International Symposium on Intelligent Signal Processing,* 1–6. https://doi.org/10.1109/WISP.2011.6051713

Halász, G., & Malachi, Y. (2014). Solar energy from Negev desert, Israel: Assessment of power fluctuations for future PV fleet. *Energy for Sustainable Development, 21,* 20–29. https://doi.org/10.1016/j.esd.2014.04.005

Hoff, T. E., & Perez, R. (2010). Quantifying PV power Output Variability. *Solar Energy, 84*(10), 1782–1793. https://doi.org/10.1016/j.solener.2010.07.003

Hollands, K. G. T., D'Andrea, L. J., & Morrison, I. D. (1989). Effect of random fluctuations in ambient air temperature on solar system performance. *Solar Energy, 42*(4), 335–338. https://doi.org/10.1016/0038-092X(89)90036-4

Jain, H., Sengupta, M., Habte, A., & Tan, J. (2020). Quantifying Solar PV Variability at Multiple Timescales for Power Systems Studies. *2020 47th IEEE Photovoltaic Specialists Conference* (PVSC), 0180–0185. https://doi.org/10.1109/PVSC45281.2020.9300658

Jamaly, S. M. (2020). Engineering Sciences (Mechanical Engineering).

Kumar, D. (2021). Spatial variability analysis of the solar energy resources for future urban energy applications using Meteosat satellite-derived datasets. *Remote Sensing Applications: Society and Environment, 22,* 100481. https://doi.org/10.1016/j.rsase.2021.100481

Kumar, D. S., Maharjan, S., Albert, & Srinivasan, D. (2022). Ramp-rate limiting strategies to alleviate the impact of PV power ramping on voltage fluctuations using energy storage systems. *Solar Energy, 234,* 377–386. https://doi.org/10.1016/j.solener.2022.01.059

Lan, H., Yin, H., Hong, Y.-Y., Wen, S., Yu, D. C., & Cheng, P. (2018). Day-ahead spatio-temporal forecasting of solar irradiation along a navigation route. *Applied Energy, 211,* 15–27. https://doi.org/10.1016/j.apenergy.2017.11.014

Lave, M., Kleissl, J., & Arias-Castro, E. (2012). High-frequency irradiance fluctuations and geographic smoothing. *Solar Energy, 86*(8), 2190–2199. https://doi.org/10.1016/j.solener.2011.06.031

Leung, C. T. (1980). The fluctuation of solar irradiance in Hong Kong. *Solar Energy, 25*(6), 485–494. https://doi.org/10.1016/0038-092X(80)90080-8

Lohmann, G. (2018). Irradiance Variability Quantification and Small-Scale Averaging in Space and Time: A Short Review. *Atmosphere, 9*(7), 264. https://doi.org/10.3390/atmos9070264

Lohmann, G. M., & Monahan, A. H. (2018). Effects of temporal averaging on short-term irradiance variability under mixed sky conditions. *Atmospheric Measurement Techniques, 11*(5), 3131–3144. https://doi.org/10.5194/amt-11-3131-2018

Lohmann, G. M., Monahan, A. H., & Heinemann, D. (2018). Local short-term variability in solar irradiance.

Luoma, J., Kleissl, J., & Murray, K. (2011). Optimal inverter sizing considering cloud enhancement. *Solar Energy, 86,* 421–429. https://doi.org/10.1016/j.solener.2011.10.012

Madanchi, A., Absalan, M., Lohmann, G., Anvari, M., & Reza Rahimi Tabar, M. (2017). Strong short-term non-linearity of solar irradiance fluctuations. *Solar Energy, 144,* 1–9. https://doi.org/10.1016/j.solener.2017.01.008

Majzoobi, A., & Khodaei, A. (2016). Application of microgrids in addressing distribution network net-load ramping. *2016 IEEE Power & Energy Society Innovative Smart Grid Technologies Conference* (ISGT), 1–5. https://doi.org/10.1109/ISGT.2016.7781276

Mbaye, A. (2022). Review on Energy Audit: Benefits, Barriers, and Opportunities. *American Journal of Energy and Natural Resources, 1*(1), Article 1. https://doi.org/10.54536/ajenr.v1i1.1054

Mills, A. (2011). Understanding Variability and Uncertainty of Photovoltaics for Integration with the Electric Power System.

Mucomole, F. V., Silva, C. A. S., & Magaia, L. L. (2023). Temporal Variability of Solar Energy Availability in the Conditions of the Southern Region of Mozambique. *American Journal of Energy and Natural Resources, 2*(1), Article 1. https://doi.org/10.54536/ajenr.v2i1.1311

Ocácia, G. C., & Santos, J. C. V. dos. (2008). Efeito de capacidade e de compensação na utilização de energia fotovoltaica e de energia eólica. *Revista Liberato, 9*(12), Article 12.

Park, J.-S., Katagi, T., Yamamoto, S., & Hashimoto, T. (2001). Operation control of photovoltaic/diesel hybrid generating system considering fluctuation of solar radiation. *Solar Energy Materials and Solar Cells,* *67*(1), 535–542. https://doi.org/10.1016/S0927-0248(00)00325-1

Perez, M. J. R., & Fthenakis, V. M. (2015). On the spatial decorrelation of stochastic solar resource variability at long timescales. *Solar Energy, 117,* 46–58. https://doi.org/10.1016/j.solener.2015.04.020

Perez, R., David, M., Hoff, T. E., Jamaly, M., Kivalov, S., Kleissl, J., Lauret, P., & Perez, M. (2016). Spatial and Temporal Variability of Solar Energy. *Foundations and Trends® in Renewable Energy, 1*(1), 1–44. https://doi.org/10.1561/2700000006

Perez, R., Rábago, K. R., Trahan, M., Rawlings, L., Norris, B., Hoff, T., Putnam, M., & Perez, M. (2016). Achieving very high PV penetration – The need for an effective electricity remuneration framework and a central role for grid operators. *Energy Policy, 96,* 27–35. https://doi.org/10.1016/j.enpol.2016.05.016

Perpiñán, O., & Lorenzo, E. (2011). Analysis and synthesis of the variability of irradiance and PV power time series with the wavelet transform. *Solar Energy, 85*(1), 188–197. https://doi.org/10.1016/j.solener.2010.08.013

Perr, C. A. (1994). Solar-irradiance variations and regional precipitation fluctuations in the Western USA. *International Journal of Climatology, 14*(9), 969–983. https://doi.org/10.1002/joc.3370140903

Quoc Hung, D., & Mishra, Y. (2019). Voltage fluctuation mitigation: Fast allocation and daily local control of DSTATCOMs to increase solar energy harvest. *IET Renewable Power Generation, 13*(14), 2558–2568. https://doi.org/10.1049/iet-rpg.2019.0223

Rapti, A. S. (2000). Atmospheric transparency, atmospheric turbidity and climatic parameters. *Solar Energy, 69*(2), 99–111. https://doi.org/10.1016/S0038-092X(00)00053-0

Sha, A., & Aiello, M. (2018). Topological Considerations on Decentralised Energy Exchange in the Smart Grid. *Procedia Computer Science, 130,* 720–727. https://doi.org/10.1016/j.procs.2018.04.126

Sha, A., & Aiello, M. (2020). Topological considerations on peer-to-peer energy exchange and distributed energy generation in the smart grid. *Energy Informatics, 3*(1), 8. https://doi.org/10.1186/s42162-020-00109-5

Siebentritt, S. (2011). What limits the efficiency of chalcopyrite solar cells? *Solar Energy Materials and Solar Cells, 95*(6), 1471–1476. https://doi.org/10.1016/j.solmat.2010.12.014

Soubdhan, T., Emilion, R., & Calif, R. (2009). Classification of daily solar radiation distributions using a mixture of Dirichlet distributions. *Solar Energy, 83*(7), 1056–1063. https://doi.org/10.1016/j.solener.2009.01.010

Suri, M., Huld, T., Dunlop, E., Albuisson, M., Lefèvre, M., & Wald, L. (2007). Uncertainties in solar electricity yield prediction from fluctuation of solar radiation.

Syed, M. A., & Khalid, M. (2021). Neural network predictive control for smoothing of solar power fluctuations with battery energy storage. *Journal of Energy Storage, 42,* 103014. https://doi.org/10.1016/j.est.2021.103014

Tiba, C., Ramalho, R. D., Souza, J. L. de, & Silva, M. A. de A. da. (2016). VARIABILIDADE DA IRRADIAÇÃO SOLAR EM ESCALA DE MINUTO NO ESTADO DE ALAGOAS. Anais Congresso Brasileiro de Energia Solar - CBENS, 1–7. https://doi.org/10.59627/cbens.2016.1454

Trapero, J. R., Kourentzes, N., & Martin, A. (2015). Short-term solar irradiation forecasting based on Dynamic Harmonic Regression. Energy, 84, 289–295. https://doi.org/10.1016/j.energy.2015.02.100

Tu, C.-Y. (1987). A solar wind model with the power spectrum of Alfvénic fluctuations. *Solar Physics, 109*(1), 149–186. https://doi.org/10.1007/BF00167405

Twidell, J., & Weir, T. (2015). Renewable Energy Resources (3rd ed.). Routledge. https://doi.org/10.4324/9781315766416

Woyte, A., Belmans, R., & Nijs, J. (2007). Fluctuations in instantaneous clearness index: Analysis and statistics. *Solar Energy, 81*(2), 195–206. https://doi.org/10.1016/j.solener.2006.03.001

Woyte, A., Belmans, R., & Nijs, J. (2007). Localized Spectral Analysis of Fluctuating Power Generation from Solar Energy Systems. *EURASIP Journal on Advances in Signal Processing, 2007*(1), 080919. https://doi.org/10.1155/2007/80919

Woyte, A., Van Thong, V., Belmans, R., & Nijs, J. (2006). Voltage fluctuations on distribution level introduced by photovoltaic systems. *IEEE Transactions on Energy Conversion, 21*(1), 202–209. https://doi.org/10.1109/TEC.2005.845454

Zhang, S., & Yan, Y. (2022). Thermal performance of latent heat energy storage system with/without enhancement under solar fluctuation for Organic Rankine power cycle. *Energy Conversion and Management, 270,* 116276. https://doi.org/10.1016/j.enconman.2022.116276

Zheng, J., Du, J., Wang, B., Klemeš, J. J., Liao, Q., & Liang, Y. (2023). A hybrid framework for forecasting power generation of multiple renewable energy sources. *Renewable and Sustainable Energy Reviews, 172,* 113046. https://doi.org/10.1016/j.rser.2022.113046

Zhou, Y., Meng, X., Belle, J. H., Zhang, H., Kennedy, C., Al-Hamdan, M. Z., Wang, J., & Liu, Y. (2019). Compilation and spatio-temporal analysis of publicly available total solar and UV irradiance data in the contiguous United States. *Environmental Pollution, 253,* 130–140. https://doi.org/10.1016/j.envpol.2019.06.074